A novel approach for seismoelectric measurements using multielectrode arrangements – I: theory and numerical experiments

Michel Dietrich, M Devi, Stéphane Garambois, Daniel Brito, Clarisse Bordes

submitted to *Geophys. J. Int.*

A novel approach for seismoelectric measurements using multi-electrode arrangements: I – Theory and numerical experiments

M. Dietrich[1⋆], M. S. Devi[1], S. Garambois[1], D. Brito[2] and C. Bordes[2]

[1] *Univ. Grenoble Alpes, Univ. Savoie Mont Blanc, CNRS, IRD, IFSTTAR, ISTerre, 38000 Grenoble, France*

[2] *Univ. de Pau et des Pays de l'Adour, CNRS, TOTAL, LFCR-IPRA, 64000 Pau, France*

1 SUMMARY

Seismoelectric measurements consist in recording the transient electric fields generated by seismic waves propagating in fluid-filled porous or fractured media. The electric fields are conventionally measured by voltage differences between two closely spaced electrodes. Unfortunately, this measurement protocol has a direct influence on the recorded waveforms and their amplitudes. Using a filter theory approach and full waveform numerical simulations of the coupled seismic and electromagnetic wave propagation in fluid-filled porous media, we show that the coseismic electric arrivals and the small-amplitude electromagnetic interface response can be severely distorted and/or attenuated by conventional surface electrode layouts. Unlike the low-pass wavenumber filter representing the response of two geophones connected in series, the filter associated with a voltage difference is shown to be a band-pass wavenumber filter. As a result, not only horizontally and obliquely propagating waves but also vertically propagating waves undergo selective frequency attenuation in the 0–150 Hz frequency band used in field surveys. It is shown that electrode spacing cannot be optimized to enhance the electric signature of typical seismic reflections and electromagnetic interface responses, neither with horizontal dipoles nor with reasonably sized vertical dipoles. To mitigate the damaging filtering effects of electric dipoles, we consider arrangements of 3 and 5 equidistant electrodes

with alternating polarity and generalize these configurations to a higher odd number of electrodes. We show that such arrangements are ideally described by low-pass wavenumber filters which preserve the quasi-plane waves corresponding to the electromagnetic interface responses in the frequency band of interest. These properties are entirely confirmed by the computation of synthetic seismoelectrograms representing the electric potential created by a seismic excitation, which allow us to determine voltage differences or voltage combinations involving two or more electrodes. In field conditions, these benefits can be challenged by the imperfect coupling between the electrodes and the ground, or by a misplacement of the electrodes, both of which require a strict control of the electrode installation.

2 INTRODUCTION

Seismoelectric signals are obtained by firing a seismic source and by recording the transient electric fields resulting from the seismic wave propagation in fluid-filled porous or fractured media. Simple metallic rods driven into moist soil and connected as electric dipoles to a recording instrument usually suffice to detect the dominant contributions of the seismoelectric response (Thompson & Gist 1993; Mikhailov et al. 1997; Beamish 1999). The latter consist of electric fields mimicking the seismic surface waves and compressional body waves recorded on seismic sections. These coseismic effects, however, carry only information about the properties of the medium surrounding the receivers as they merely correspond to electric fields traveling with the seismic waves with no radiation outside the wave pulses (Pride & Haartsen 1996). A second observation has received much more attention because of its potential use for the remote detection and characterization of fluids contained in porous geological formations: seismic waves crossing interfaces at depth generate fast propagating electromagnetic (EM) disturbances which are also likely to be captured by the electric dipoles deployed at the ground surface. Referred to as interface response, these events show up as subhorizontal plane-waves arriving at approximately half the two-way traveltime of their seismic counterparts. Their properties were described theoretically by Pride & Haartsen (1996), Haartsen & Pride (1997) and Garambois & Dietrich (2002), and experimentally by Martner & Sparks (1959), Thompson & Gist (1993), Butler et al. (1996), Beamish (1999), Zhu et al. (2000), Garambois & Dietrich (2001) and Dupuis et al. (2007) to name but a few. In this short presentation of seismoelectric experiments, two major difficulties of field measurements should not be overlooked. On the one hand, the recordings are in most cases entirely dominated by power line noise at 50 Hz or 60 Hz and all their harmonics in the frequency band of interest. It has been shown that the magnitude of this noise increases more or less linearly with the

spacing between the electrodes used to measure voltage differences (Thompson 1936; Beamish 1999). This noise considerably hampers the detection of seismoelectric signals. However, as it shows narrow and stable spectral lines, and since it is mostly stationary over the record length, it can be efficiently attenuated by using specific notch filters such as the block or sinusoidal subtraction techniques proposed by Butler & Russell (1993). On the other hand, whereas coseismic effects are almost systematically recorded, many seismoelectric campaigns fail to record interface responses, because of the very weak amplitudes of these arrivals, or for reasons that are not yet fully understood (Beamish 1999). These difficulties currently limit the development of seismoelectric investigations for subsurface and reservoir characterization. Recently, Butler et al. (2018) identified quasi-coseismic arrivals in field data, which they interpreted as possibly being the evanescent EM waves predicted by Ren et al. (2015) from numerical simulations. Such observations underline the variety of forms that electrokinetic effects may take in practical applications. A good deal of hope has been pinned on the reciprocal electroseismic exploration technique, whereby seismic wave fields are created by the generation and propagation of EM waves in the subsurface. This approach, too, still needs to prove itself in spite of innovative developments and encouraging results (Hornbostel & Thompson 2007; Thompson et al. 2007). Both types of data acquisition, seismoelectric or electroseismic, generally require powerful sources and sensitive receivers since the detection of converted waves is considerably impeded by their weak amplitudes. Signal-to-noise enhancement and improved detection of EM interface responses remain major issues for the effective use of these techniques. For a recent review of seismoelectromagnetic phenomena of electrokinetic origin, we refer the reader to the book of Revil et al. (2015).

In this paper, we question the procedure used for measuring electric fields in seismoelectric surveys. These measurements are conventionally done with electrode pairs deployed along linear profiles, symmetrically with respect to the location of the seismic source. The electric dipoles are connected to a digitizer, preferably one that has a high input impedance and high common mode rejection (Beamish 1999). The central idea expressed in this article is that electric dipole measurements are likely to strongly attenuate the interfacial EM conversions and other important components of the seismoelectric response, for the simple reason that voltage differences largely cancel out arrivals showing little or no delay at the electrodes.

Quantitative investigations are therefore in order to understand the relationships between electrode arrangements and seismoelectric waveforms. We will specifically investigate multi-electrode arrays to measure electric fields, aiming in particular at enhancing interfacial effects with respect to coseismic arrivals. We start by using a filter theory approach to determine the

frequency response of electric dipoles and specific multi-electrode arrangements that preserve the information content of the interface responses. The solution retained is directly inspired from the work of Thompson (1936) which was carried out for a related yet different field application since Thompson's goal was to detect transient changes of electrical resistivity due to the passage of seismic waves. The proposed electrode layouts bear some resemblance to the multilayer capacitors used in electronics. However, the use of an odd number of electrodes results in distinct advantages, notably the possibility to estimate electric potentials rather than electric fields for certain types of waves. The ideas put forward with the filter theory approach are subsequently confirmed and amplified in the second part of this article, by means of full waveform numerical simulations of seismoelectric signals in stratified fluid-filled poro-elastic media. Simple modifications of the computer code of Garambois & Dietrich (2002) allow us to evaluate the electric potential from the electric field, and from there, to implement the filters introduced previously by enabling the calculation of voltage differences or voltage combinations implying two or more electrodes. The validity of our approach is further confirmed in a companion paper presenting laboratory measurements (Devi et al. 2018).

3 A FILTER THEORY APPROACH

The developments presented in this section show many similarities with the computation of the frequency response of a group of geophones connected in series and planted at constant intervals (Johnson 1939; Lombardi 1955; Vermeer 2002). Here, we restrict ourselves to linear antennas of receivers deployed inline with the direction of the profile. In onshore reflection seismics, groups of geophones are commonly employed to enhance reflected waves reaching the ground surface almost vertically, while attenuating at the same time surface waves propagating horizontally. The tuning of the array is obtained by selecting a number N of geophones and their spacing d. The frequency response of the receiver antenna is usually evaluated by assuming that the incoming waves are plane waves propagating in the (x, z) plane at a constant speed V with an angle θ, as shown in Fig. 1a. With these assumptions, the apparent velocities of the wavefront along the horizontal and vertical directions are

$$V_{ax} = \frac{V}{\sin\theta} \quad \text{and} \quad V_{az} = \frac{V}{\cos\theta}. \tag{1}$$

3.1 Horizontal electric dipoles

Let us now consider a seismoelectric experiment in which the received time-vaying electric field $E(t)$ associated with an incoming seismic plane wave is measured by a voltage difference

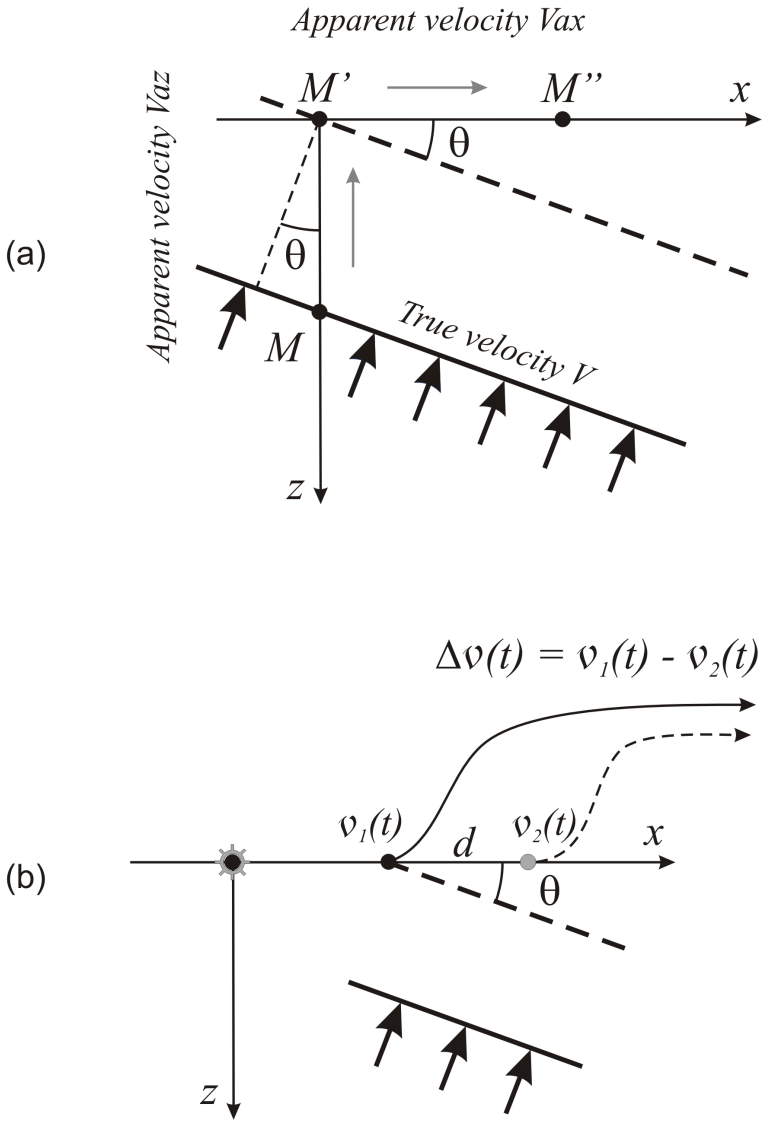

Figure 1 (a) Horizontal and vertical apparent velocities of a plane wave propagating in-plane at velocity V with an angle of incidence θ. (b) Estimation of the electric field associated with a seismic plane-wave from the voltage difference measured between two electrodes spaced a distance d apart.

$\Delta v(t)$ between two electrodes located at the ground surface (Fig. 1b), i.e.,

$$E(t) \simeq \frac{\Delta v(t)}{d} = \frac{v_1(t) - v_2(t)}{d} = \frac{v_1(t)}{d} * [\,\delta(t) - \delta(t - \tau_x)\,] \tag{2}$$

where $v_1(t)$ is the voltage received at the electrode closest to the source and $\tau_x = d/V_{ax} = d \sin\theta / V$ is the time delay of the plane wave between the two electrodes. $\delta(t)$ is the Dirac delta function and symbol $*$ denotes the convolution operator. In the frequency domain, the

electric field $\mathcal{E}(f)$ measured by the dipole writes

$$\mathcal{E}(f) \simeq \frac{\vartheta_1(f)}{d} \left[1 - e^{-i2\pi\tau_x f} \right] \tag{3}$$

where f denotes the frequency and $\vartheta_1(f)$ is the Fourier transform of $v_1(t)$.
Factorizing $\exp(-i\pi\tau_x f)$ in eq. (3), we obtain

$$\mathcal{E}(f) \simeq \frac{\vartheta_1(f)}{d}\, G_{2el}(f) \tag{4}$$

where the complex gain of the filter associated with the voltage difference is

$$G_{2el}(f) = 2\, i\, e^{-i\pi\tau_x f}\, \sin(\pi\tau_x f) \tag{5}$$

and whose modulus writes

$$|\, G_{2el}(f)\,| = 2\, |\sin(\pi\tau_x f)|\,. \tag{6}$$

The zeroes of filter $|G_{2el}(f)|$ are then given by

$$f_{0m} = \frac{m}{\tau_x}\,;\; m = 0, 1, 2, \ldots \tag{7}$$

The dc component ($f = 0$) of the records is obviously eliminated because of the subtraction of two identical quantities. Between the zero frequency and the first zero $f_{01} = 1/\tau_x$, the first lobe of $|G_{2el}(f)|$ depicts a band-pass filter having a maximum value of 2 at $f_{max_1} = 1/2\tau_x = V/2d\sin\theta$. The dipole aperture can inversely be tuned for that particular frequency by adopting the electrode spacing

$$d_{opt} = \frac{V}{2f_{max_1}} \cdot \frac{1}{\sin\theta} = \frac{\lambda_{min}}{2} \cdot \frac{1}{\sin\theta} \tag{8}$$

where λ_{min} is the minimum wavelength of the incoming wave. It is readily seen that for a plane-wave arriving more or less parallel to the ground surface ($\theta \simeq 0$), the optimum electrode spacing would be unacceptably large to meet this criterion.
By comparison, the magnitude of the filter corresponding to the output of two geophones connected in series at an interval d is

$$|\, G_{2s}(f)\,| = 2\, |\cos(\pi\tau_x f)| \tag{9}$$

because the minus sign in eq. (3) is then replaced by a plus sign. The above expression indicates that the first lobe of function $|G_{2s}(f)|$ is a low-pass filter limited by the cut-off frequency $f'_{01} = 1/2\tau_x$. Fig. 2 displays the magnitudes of the filters $G_{2el}(f)$ and $G_{2s}(f)$ for two receivers (electrodes or geophones) spaced 5 m apart, and two apparent velocities of the wavefront along the ground surface, $V_{ax} = 200$ m/s and $V_{ax} = 5400$ m/s. The first apparent velocity typically corresponds to a Rayleigh wave propagating along the ground surface ($V = 200$ m/s, $\theta = 90°$) whereas the second situation represents, for example, a plane wave traveling at

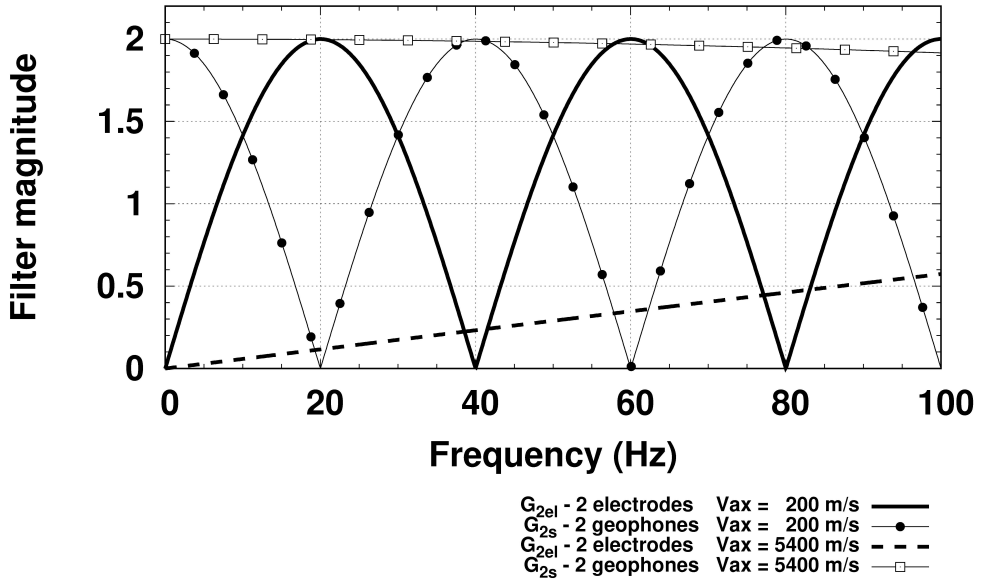

Figure 2 Comparison of the filter responses $|G_{2el}(f)|$ and $|G_{2s}(f)|$ corresponding to an electric dipole (subtraction of two signals) and to an array of two geophones connected in series (addition of two signals) for two incoming plane waves having different incident angles (see text). In both cases, the two receivers are spaced 5 m apart.

$V = 1800$ m/s with an angle of incidence $\theta \simeq 19.5°$. Filter amplitudes greater than 1 mean that the incoming waves will be amplified in the measurement process whereas amplitudes smaller than 1 lead to an attenuation of these waves. It is easily demonstrated from eq. (6) (see Appendix A) that the frequency limits of these two regimes inside the first lobe are $[1/6\tau_x, 5/6\tau_x]$. With the numerical values adopted in our example, the electric signature of the 200 m/s surface wave is well recorded by the dipoles, and is even enhanced within the frequency interval $[\,6.67, 33.35\,]$ Hz. On the other hand, waves propagating towards the surface with small angles of incidence, small time delays τ_x, are severely attenuated as the filter takes the form of a long ramp $|G_{2el}(f)| \simeq \pi\tau_x f$ at low frequencies because the maximum of the filter occuring at $f_{max_1} = 1/2\tau_x$ is then shifted towards very high frequencies. This behaviour strongly differs from that of filter $|G_{2s}(f)|$ derived for a pair of geophones, which maintains an amplitude close to one for small angles of incidence, therefore favouring reflections from flat lying beds in seismic reflection surveys.

3.2 Vertical electric dipoles

One may wonder, in this situation, if vertical electric dipoles would do a better job to capture and enhance the interface response which is considerably diminished on records performed with

horizontal dipoles. Vertical dipoles cannot easily be installed in field, and for that reason, they are notably absent in magnetotelluric surveys. As we are still dealing with a voltage difference, the filtering effect of vertical dipoles is described by the same equations as those introduced before for horizontal dipoles. However, we must now consider the apparent velocity V_{az} of the wavefront along the vertical direction and replace the delay time τ_x by its counterpart $\tau_z = d/V_{az} = d\cos\theta/V$. The first lobe of the filter defines, as before, a band-pass filter between frequencies 0 and $f_{01} = 1/\tau_z = V/d\cos\theta$ with a maximum amplitude of 2 at $f_{max_1} = 1/2\tau_z$. Simple numerical applications of these formulas show that vertical dipoles are not a better configuration to boost the interface response in seismoelectric measurements, mainly because the very high velocities of the EM waves generated at the interfaces result in very small values of the delay time τ_z.

These simple considerations clearly point to the fact that the electrode spacing cannot be optimized to enhance the electric signature of typical seismic reflections and electromagnetic interface response in the 0–150 Hz frequency range used for the exploration of the subsurface. This is not possible neither with horizontal dipoles nor with vertical dipoles as it would require unrealistically large dipoles with electrodes spaced a few tens of meters apart, a situation in which the plane-wave approximation of incident waves is usually no longer valid. Only the coseismic surface waves can, to some degree, be enhanced with horizontal dipoles, although this may be challenged when velocity dispersion is important. The quasi-plane waves associated with the interface response of a horizontally stratified medium are substantially attenuated in the measurement process.

3.3 Multi-electrode arrangements

In his 1936 Geophysics paper on "The seismic electric effect", Thompson (1936) considered linear arrays of electrodes to reduce the electric noise in a pioneering attempt to measure the change of resistivity of the subsurface due to the passage of seismic waves and accompanying elastic deformation. In addition to using conventional electric dipoles, he introduced configurations involving 3 and 5 electrodes and observed a significant reduction of noise with the latter. These multi-electrode arrangements are represented in Fig. 3. For the 3-electrode set-up, for instance, Thompson (1936) mentioned that "the two outside electrodes are connected together and are of one polarity while the center electrode is of the opposite polarity". He described the electrode configurations but did not write any equations to characterize their effect on electric fields.

The regularly-spaced electrode configurations used by Thompson (1936) turn out to be

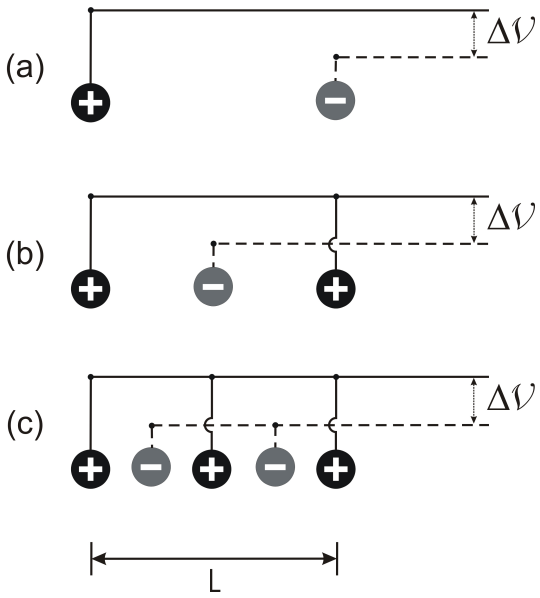

Figure 3 (a) Conventional electric dipole, (b) 3-electrode and (c) 5-electrode configurations used by Thompson (1936). L is the total aperture of the electrode antennas.

especially useful for our objective of enhancing the interface response in seismoelectric surveys. Indeed, the mathematical responses of the 3- and 5-electrode arrangements can be written in the time domain as

$$s_{3el}(t) = v_1(t) + v_3(t) - v_2(t) \simeq 2v_2(t) - v_2(t) = v_2(t) \tag{10}$$

$$s_{5el}(t) = v_1(t) + v_3(t) + v_5(t) - v_2(t) - v_4(t) \simeq 3v_3(t) - 2v_3(t) = v_3(t) \tag{11}$$

by numbering the electrodes in Fig. 3 from left to right, for example. In the right hand sides of the two above equations, we have implicitly used the arithmetic means of voltages considered to be symmetric relative to the centre of the electrode arrays. These approximations will most likely hold true for plane waves arriving parallel to the ground surface as long as the amplitude variations of the signals picked up by the electrodes remain small over the aperture of the receiving antennas. By doing so, we highlight the fact that, in spite of still being measurements of voltage differences, the electrode arrangements introduced by Thompson (1936) yield signals that are closely related to the *electric potential* in the middle of the antennas rather than being a true *electric field*. Multi-electrode arrays are therefore capable of removing the differential aspects of dipole measurements, with some important consequences that will be presented in the next sections.

We demonstrate in Appendix A that the filters achieved by the 3- and 5-electrode arrays

depicted in Fig. 3 are expressed in the Fourier domain as

$$|\,G_{3el}(f)\,| \;=\; |2\cos(\pi\tau f) - 1| \;=\; \left|\frac{\cos(3\,\pi\tau f/2)}{\cos(\pi\tau f/2)}\right| \quad \text{and} \tag{12}$$

$$\begin{aligned} |\,G_{5el}(f)\,| \;&=\; |2\cos(\pi\tau f) - 2\cos(\pi\tau f/2) + 1| \;=\; \left|4\cos^2(\pi\tau f/2) - 2\cos(\pi\tau f/2) - 1\right| \\ &=\; \left|\frac{\cos(5\,\pi\tau f/4)}{\cos(\pi\tau f/4)}\right|. \end{aligned} \tag{13}$$

The general formula for an electrode array consisting of an odd number N of electrodes alternatively connected with positive and negative polarities is shown to be

$$|\,G_{Nel}(f)\,| \;=\; \left|\frac{\cos\left(\pi\tau f\,\dfrac{N}{N-1}\right)}{\cos\left(\pi\tau f\,\dfrac{1}{N-1}\right)}\right|. \tag{14}$$

This expression bears some similarity to the formula derived for a linear, non-weighted array of N geophones connected in series, whose response may be expressed as the ratio of two sine functions (see, e.g., Vermeer 2002). Here, we have written the time delay τ without subscript since the above formulas apply equally to horizontal and vertical arrays as noted before for the dipole configuration. In the following, we will only consider horizontal arrays. It is also important to note that τ represents the time delay of the incoming plane wave across the entire aperture of the electrode array: $\tau = L/V_{ax}$. If the electrodes are spaced a distance d apart, $L = d$ for the dipole, $L = 2d$ for the 3-electrode array, and $L = 4d$ for the 5-electrode array. The convention adopted in this paper is to consider fixed-length electrode arrays by subdividing the array length L into smaller intervals when the number of electrodes increases. Another option would have been to consider a fixed electrode interval d so that increasing the number of electrodes would result in longer arrays. The latter situation is represented by a slightly different mathematical formulation not given here. In Appendix A, we derive additional properties of the filters which are summarized in Table 1 and illustrated in Fig. 4.

The most important property to be noted from Fig. 4 is that the 3- and 5-electrode filter responses now show the desired low-pass behaviour in their first lobe. They are also very similar in that frequency range. As a consequence, plane-wave arriving parallel to the ground surface will be preserved and properly recorded with these electrode arrangements. In addition, compared to the classical dipole configurations, 3- and 5-electrode arrays have the potential to amplify the recorded signals: the amplitudes may be increased threefold with three electrodes, and fivefold with 5 electrodes, although only in specific frequency bands (Fig. 4a). This particular property cannot be easily exploited in field measurements, but could prove useful in laboratory experiments which offer more flexibility with the use of acoustic sources operating in specific frequency ranges (see our companion paper Devi et al.

Nb Electrodes	$\|G(0)\|$	$\|G(f_{max})\|$	f_{max_1}	f_{01}	f_{02}	f_{03}
2 [+.....−]	0	2	$1/2\tau$	$1/\tau$	$2/\tau$	$3/\tau$
3 [+..... − .....+]	1	3	$1/\tau$	$1/3\tau$	$5/3\tau$	$7/3\tau$
5 [+. − . + . − .+]	1	5	$2/\tau$	$2/5\tau$	$6/5\tau$	$14/5\tau$
$N = 7, 9, 11, 13 \ldots$	1	N	$(N-1)/2\tau$	$(N-1)/2N\tau$	see	Appendix A

Table 1 Main properties of the filters corresponding to combinations of 2, 3, 5 and arbitrary odd number N electrodes. $|G(0)|$ is the magnitude of the filter at zero frequency, $|G(f_{max})|$ is the absolute maximum amplitude of the filter, f_{max_1} is the first frequency corresponding to the absolute maximum amplitude of the filter, and f_{01}, f_{02} and f_{03} are the frequencies corresponding to the first three notches of the filter.

2018). Finally, it should be noted that the 3- and 5-electrode schemes displayed in Fig. 3 can easily be generalized to a higher number of electrodes using the same alternating connection pattern: by considering an odd number N of electrodes, $N = 3, 5, 7 \ldots$, the amplification achieved by the associated filter reaches a maximum value of N. This result is demonstrated in Appendix A. Except for this advantage, and considering the similarity of the responses of 3- and 5-electrode arrays in the first lobe, the use of configurations involving a large number of elements seems to be of marginal interest in practice as it would require installing a great many receivers.

Fig. 5 displays, as a function of frequency, the theoretical amplification ratio that may be achieved with a 3-electrode array compared to a dipole. These results were obtained for a plane-wave showing almost no moveout ($V_{ax} = 100\,000$ m/s) typically representing an interface response, and for four different array lengths ranging from 1 to 10 m. It is seen that the estimated amplifications can be quite large for single frequencies. However, they will be less important for broad-band signals as shown later in the numerical simulations.

3.4 Poorly grounded electrodes

In the previous section, we have described and emphasized the significant advantages of using multi-electrode arrays for recording seismoelectric events, especially the quasi plane waves corresponding to an interface response. While true in theory, these advantages must nevertheless be tempered in field conditions because of potential electrical imbalances within the electrode arrays. The latter will mostly originate from poor ground coupling affecting the electrode

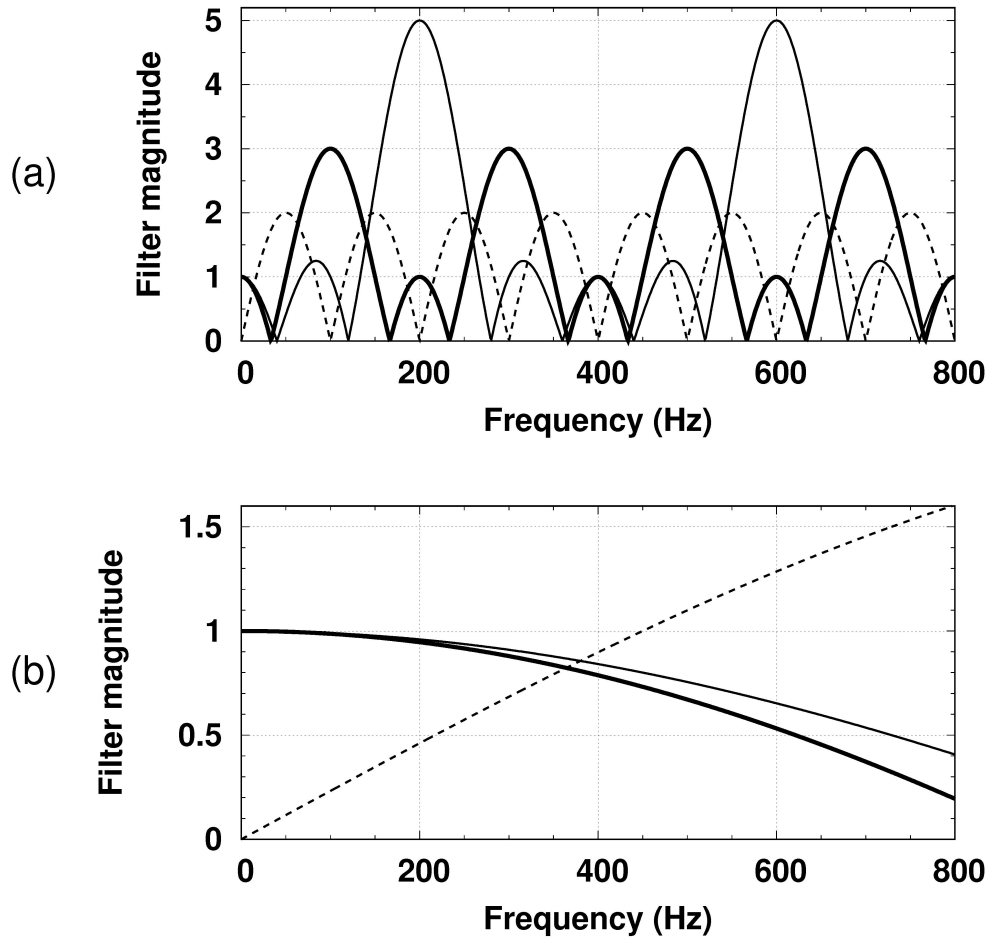

Figure 4 Filter responses of 2-, 3- and 5-electrode arrangements having an aperture of 2 m, for incoming plane waves with horizontal apparent velocities of (a) 200 m/s and (b) 5400 m/s. The dipole responses are displayed in dashed lines, the 3- and 5-electrode configurations are represented as thick and thin solid lines, respectively.

contact resistance, as mentioned already by Thompson (1936) in his original paper. Other factors related to defective connectors or faulty wiring are likely to undermine the theoretical benefits of the proposed data acquisition scheme as well.

In other words, the equations developed so far rely on the hypothesis that the multiple electrodes involved in a receiving array are accurately measuring the electric potentials in an identical manner, i.e., they are ideally grounded. When this is not the case, the potential recorded by each electrode is affected by a complex, frequency-dependent weighting function. Papers dealing with such effects are scarce but can be found in the field of electromagnetic prospecting. Thus, Zonge & Hughes (1985) developed an equivalent RLC circuit model to estimate the electric field magnitude as a function of frequency for various electrode contact

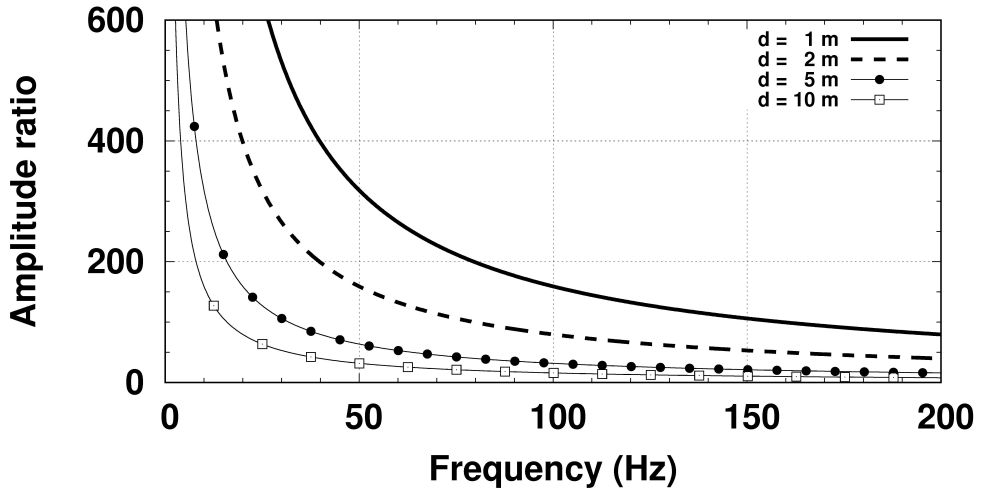

Figure 5 Theoretical amplitude ratio between the 3-electrode response $|G_{3el}(f)|$ and dipole response $|G_{2el}(f)|$ for an incoming plane-wave having an apparent velocity of 100 000 m/s along the ground surface, for four different apertures of electrode antennas.

resistances. In the following, we investigate the consequences of such weighting functions on the filters previously defined, by restricting ourselves to frequency-independent and real factors for a first assessment of their influence on the filter performance.

For the dipole configuration, we consider a modified filter from eq. (3) with parametric weighting factors w_1 and w_2

$$\begin{aligned} \left| G'_{2el}(f) \right| = \left| w_1 - w_2\, e^{-i2\pi\tau f} \right| &= \left\{ \left[w_1 - w_2 \cos(2\pi\tau f) \right]^2 + \left[w_2 \sin(2\pi\tau f) \right]^2 \right\}^{1/2} \\ &= \left[w_1^2 - 2 w_1 w_2 \cos(2\pi\tau f) + w_2^2 \right]^{1/2} . \end{aligned} \tag{15}$$

The ideally grounded electrodes correspond to equal weighting factors $w_1 = w_2 = 1$.

Fig. 6 presents the modified filter response of 5 m dipole configurations according to eq. (15). When the weighting factors are equal in magnitude and have the same sign, the shape of filter $|G'_{2el}(f)|$ is similar to that of filter $|G_{2el}(f)|$ displayed in Fig. 2 except for a general scaling in amplitude. However, when there is a mismatch between w_1 and w_2, we observe that filter $|G'_{2el}(f)|$ is somewhat improved in the sense that it no longer shows notches. When w_1 and w_2 have opposite sign, filter $|G'_{2el}(f)|$ resembles filter $|G_{2s}(f)|$ introduced in eq. (9) for the sum of two receiver outputs. Finally, it can be shown that $\max |G'_{2el}(f)| = |w_1 + w_2|$; $\min |G'_{2el}(f)| = |w_1 - w_2|$ when $w_1 w_2 > 0$, and vice-versa when $w_1 w_2 < 0$: in that case, $\min |G'_{2el}(f)| = |w_1 + w_2|$ and $\max |G'_{2el}(f)| = |w_1 - w_2|$.

For the 3-electrode configuration, we consider a modified filter including weighting factors

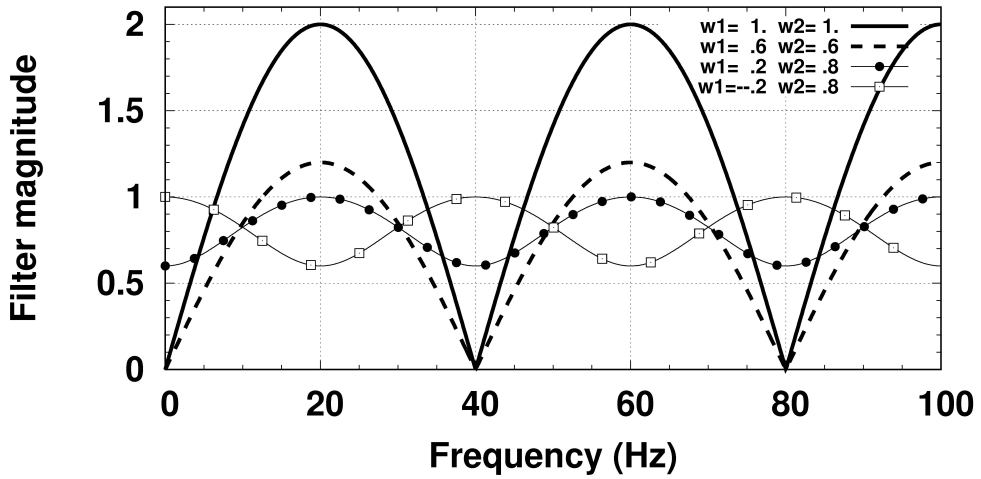

Figure 6 Modified filter responses of dipole configurations having an aperture of 5 m obtained with several combinations of weighting factors $\{w_1,w_2\}$: $\{1.,1.\}$,$\{.6,.6\}$, $\{.2,.8\}$ and $\{-.2,.8\}$.

w_1, w_2 and w_3:

$$\begin{aligned} \left| G'_{3el}(f) \right| &= \left| w_1 - w_2\, e^{-i\pi\tau f} + w_3\, e^{-i2\pi\tau f} \right| \\ &= \left[{w_1}^2 + {w_2}^2 + {w_3}^2 + 2\, w_1 w_3 \cos 2\pi\tau f - 2\, w_2(w_1 + w_3) \cos \pi\tau f \right]^{1/2}. \end{aligned} \tag{16}$$

As before, the ideally grounded electrodes correspond to $w_1 = w_2 = w_3 = 1$. The modified filter responses computed for an aperture of 5 m are displayed in Fig. 7. We observe again that equal values of w_1, w_2 and w_3 merely lead to scaled versions of the original $|G_{3el}(f)|$ filter. On the contrary, a singular situation arises when $w_1 - w_2 + w_3 = 0$. This case is illustrated in Fig. 7 with $w_1 = .3$, $w_2 = .8$ and $w_3 = .5$. In such situations, the 3-electrode array behaves like a dipole and is characterized by a band-pass filter effect at low frequencies. When the weighting factors are all positive or if they are all negative, the maximum amplitude of the filter is given by $\max |G'_{3el}(f)| = |w_1 + w_2 + w_3|$. In all situations, the filter amplitude at zero frequency is equal to $|G'_{3el}(0)| = |w_1 - w_2 + w_3|$.

In summary, poorly grounded electrodes will in general degrade the performance of the filters corresponding to ideally grounded electrodes. This may result in a loss of the benefits provided by multi-electrode arrays depending on the weighting that is applied to the individual electrodes. Conversely, unbalanced electrodes in a dipole configuration may improve the measurement of the electric field. It is therefore necessary, whenever possible, to assess the electrode contact resistance in field experiments to account for potential imbalances. A full control of these effects would make it possible to fine-tune the electrode arrays beyond what has been presented here.

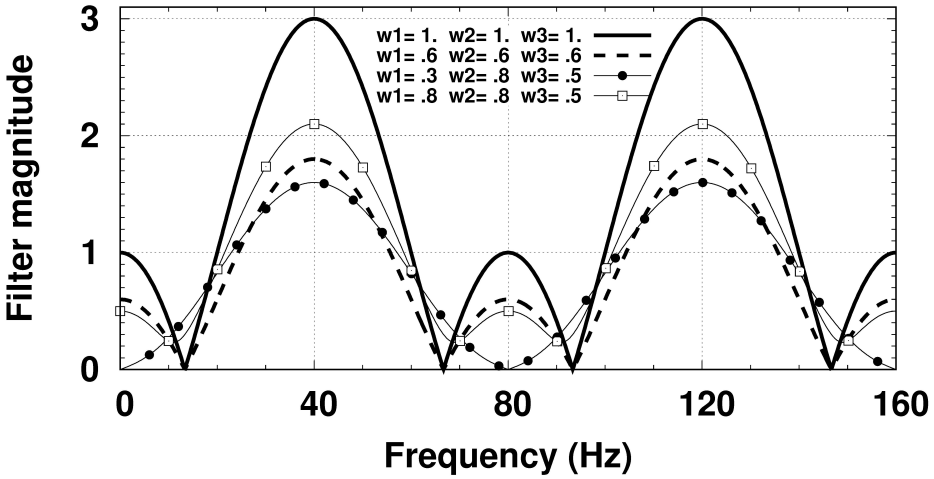

Figure 7 Modified filter responses of 3-electrode configurations having an aperture of 5 m obtained with several combinations of weighting factors $\{w_1, w_2, w_3\}$: $\{1., 1., 1.\}$,$\{.6, .6, .6\}$, $\{.3, .8, .5\}$ and $\{.8, .8, .5\}$.

4 FULL WAVEFORM NUMERICAL SIMULATIONS

To go one step further in the development and validation of the theory introduced above for plane waves, we perform full waveform numerical simulations to account for additional wave propagation effects, especially wavefront curvature and wave interferences. We use the computer code developed by Garambois & Dietrich (2002) for the 3D coupled seismic and electromagnetic wave propagation in horizontally stratified, fluid-filled poroelastic media. This code relies on a full implementation of the theory of Pride (1994) which combines Maxwell equations with Biot-Gassmann equations, both sets of equations being coupled via two transport equations: a generalized Ohm's law and a generalized Darcy's law. The simulation programme written in 2002 provides the seismic, electric and magnetic wave fields at user-defined receiver locations at the ground surface or within the layering, but does not calculate the electric potential which is needed to evaluate the various combinations of voltage signals discussed previously. This modification of the computer code is addressed below.

4.1 Computation of electric potential

Quoting (Pride 1994, eq. 257), "if flow is being induced by applied pressure gradients and electric fields that are steady in time", then the electric field $\mathbf{E}$ is the negative gradient of the scalar electric potential Φ:

$$\mathbf{E} = -\boldsymbol{\nabla}\Phi. \quad \text{Hence,} \quad E_s = -\frac{\partial \Phi}{\partial s}, \tag{17}$$

i.e., component E_s of the electric field $\mathbf{E}$ in any particular direction s is obtained from the partial derivative of potential Φ with respect to that direction. We must therefore integrate a component of the electric field to obtain the potential Φ.

Most seismoelectric experiments are carried out by using point sources (explosives, shot gun) or vertical forces (weight-drop sources, vertical vibrators) which excite the PSVTM wave system, i.e., mechanical P- and SV-waves, the transverse magnetic component H_θ of the magnetic field, and the radial E_r and vertical E_z components of the electric field. In our simulation code, the core computations are performed in the frequency f and wavenumber k domain by using the generalized reflection and transmission matrix method of Kennett (1983). The wave fields propagated in the $f-k$ domain are then transformed to the time–distance domain by using the discrete wavenumber technique of Bouchon (1981) and a final Fourier transform with respect to frequency. As our code computes only the radial component E_r of the electric field, we will evaluate the scalar electric potential Φ from that component. In the cylindrical coordinate system adopted, where r represents the radial distance between source and receiver, and z the receiver depth, we must perform the following integration

$$\Phi(r,\theta,z;t) = \int E_r(r,\theta,z;t)\,dr + C \tag{18}$$

where C is a constant. For axially symmetric sources, the electric field has no transverse component, and E_r can formally be written as

$$E_r(r,z;t) = \int_{-\infty}^{+\infty} e^{i2\pi ft} df \int_0^{+\infty} \mathcal{E}_r(f,k,z) J_1(kr) k dk \tag{19}$$

where $\mathcal{E}_r(f,k,z)$ represents the radial component of the seismoelectrical reflectivity of the layered medium at the receiver level, and $J_1(\cdot)$ denotes the Bessel function of the first kind and order 1. From the Bessel function property (Abramowitz & Stegun 1964, eq. 9.1.28)

$$\frac{dJ_0(\xi)}{d\xi} = -J_1(\xi), \tag{20}$$

we infer that

$$\Phi(r,z;t) = -\int_{-\infty}^{+\infty} e^{i2\pi ft} df \int_0^{+\infty} \mathcal{E}_r(f,k,z)\, J_0(kr)\, dk \tag{21}$$

where we have essentially replaced $J_1(kr)\,k\,dk$ by $-J_0(kr)\,dk$ to perform the required integration of the electric field component E_r with respect to r. Eq. (20) now allows us to evaluate the electric potential Φ at any receiver position to investigate the dipole and proposed multi-electrode configurations. For seismic sources that are not axially symmetric, horizontal forces for instance, the expression of $E_r(r,z;t)$ is written in terms of Bessel functions $J_0(\xi)$ and $J_{inc}(\xi) = J_1(\xi)/\xi$ which are more difficult to integrate because their primitives involve in par-

ticular Struve and Lommel functions (Luke 1975, p. 413-427). These aspects are not further addressed in this article.

4.2 Straightforward filter implementation

As an alternative to forming linear combinations of electric potential to simulate multi-electrode arrangements from eq. (21), we may directly incorporate their filtering effects in the computer code. As mentioned earlier, our numerical scheme evaluates the full waveform seismoelectric response of a stratified medium by combining the individual responses of a large number (typically several hundreds or thousands) of plane waves in the frequency–wavenumber domain. Each of these plane waves is characterized by its horizontal wavenumber k which defines itself in terms of frequency f and apparent velocity V_{ax}, i.e., $k = 2\pi f/V_{ax} = 2\pi f \sin\theta/V$. Recalling that L is the total aperture of the electrode array, we can therefore write $\pi\tau f = kL/2$ and recast the frequency and apparent velocity filters as effective wavenumber filters.

These filters are finally implemented in their complex form by writing

$$\Psi_m(r,z;t) = -\int_{-\infty}^{+\infty} e^{i2\pi ft} df \int_0^{+\infty} \mathcal{E}_r(f,k,z)\, J_0(kr)\, \mathcal{F}_m(k,L)\, dk \;;\; m = 2,3,5,\ldots \tag{22}$$

where $\Psi_m(r,z;t)$ denotes the filtered electric potential for a configuration involving m electrodes. In the above equation,

$$\left|\begin{array}{lcll} \mathcal{F}_2(k,L) & = & 2i\,\sin(kL/2) & \text{dipole configuration} \\ \mathcal{F}_3(k,L) & = & 2\cos(kL/2) - 1 & \text{3-electrode configuration} \\ \mathcal{F}_5(k,L) & = & 2\cos(kL/2) - 2\cos(kL/4) + 1 & \text{5-electrode configuration} \end{array}\right. \tag{23}$$

where we have dropped the $\exp(-ikL/2)$ phase term in each expression to obtain estimates of the filter response in the middle of the electrode array instead of the response at the farthest end from the seismic source.

Modified filters including weighting functions can be introduced the same way. This approach of accounting for the filtering effects of multiple electrodes is theoretically equivalent to the corresponding linear combination of potentials evaluated at the receivers, namely,

$$\left|\begin{array}{lcl} \Psi_2(r) & \equiv & \Phi(r-L/2) - \Phi(r+L/2) \\ \Psi_3(r) & \equiv & \Phi(r-L/2) - \Phi(r) + \Phi(r+L/2) \\ \Psi_5(r) & \equiv & \Phi(r-L/2) - \Phi(r-L/4) + \Phi(r) - \Phi(r+L/4) + \Phi(r+L/2) \end{array}\right. \tag{24}$$

where the z and t variables have been omitted in $\Phi(\cdot)$ and $\Psi(\cdot)$ for sake of clarity. The validity of this result is discussed in Fig. 8, 9, 10 and 11 below.

4.3 Simulations of multi-electrode arrays

We consider a two-layer model whose properties are presented in Table 2. Each layer is characterized by 14 parameters concerning the microstructure of the porous medium (ϕ, k_0, $\mathcal{T}$), its solid phase (k_s, k_{fr}, G_{fr}, ρ_s, κ_s), fluid phase (k_f, ρ_f, η, C, κ_f) and temperature (T). The thickness of the upper layer is 35 m. Relevant properties estimated from the input parameters are listed in Table 3. The wave velocities and attenuation values are derived from the real and imaginary parts of the corresponding complex wave slownesses $S_\xi(f)$ according to

$$V_\xi(f) = \frac{1}{\Re\{S_\xi(f)\}} \quad \text{and} \quad Q_\xi(f) = \frac{1}{2V_\xi(f)\Im\{S_\xi(f)\}}, \tag{25}$$

where ξ is one of the wave types P_f, P_s, S, EM, namely, fast and slow P-waves, SV shear waves and EM waves, respectively. The expressions of the wave slownesses $S_\xi(f)$ can be found in Pride & Haartsen (1996) and in Haartsen & Pride (1997). The diffusive nature of the slow P-wave and EM wave is well attested by the very small values of their quality factors. The bulk density is given by $\rho = \rho_f\phi + \rho_s(1-\phi)$.

Input parameter	Layer 1	Layer 2
Depth (m)	35	–
Porosity ϕ ()	30%	20%
Permeability k_0 (m^2)	10^{-11}	10^{-12}
Tortuosity $\mathcal{T}$ ()	3	3
Solid bulk modulus k_s (GPa)	35	36
Frame bulk modulus k_{fr} (GPa)	0.4	5.0
Shear modulus G_{fr} (GPa)	0.5	7.0
Solid density ρ_s (kg/m^3)	2600	2700
Relative solid permittivity κ_s ()	4	4
Fluid bulk modulus k_f (GPa)	2.2	2.2
Fluid density ρ_f (kg/m^3)	1000	1000
Fluid viscosity η (Pa.s)	10^{-3}	10^{-3}
Fluid salinity C (mol/l)	10^{-3}	10^{-3}
Relative fluid permittivity κ_f ()	80	80
Temperature T (°K)	298	298

Table 2 Input parameters used for the numerical simulations of the seismoelectric responses presented in Fig. 8 and 9.

Computed property	Layer 1	Layer 2
Fast P-wave velocity V_{Pf} (m/s)	1859.8	2991.5
Fast P-wave quality factor Q_{Pf} ()	643.2	331 711.2
Slow P-wave velocity V_{Ps} (m/s)	86.0	75.7
Slow P-wave quality factor Q_{Ps} ()	0.6	0.5
S-wave velocity V_S (m/s)	485.8	1722.3
S-wave quality factor Q_S ()	446.0	4729.1
EM-wave velocity V_{EM} (m/s)	1 611 917.3	2 959 689.8
EM-wave quality factor Q_{EM} ()	0.5	0.5
Bulk density ρ (kg/m^3)	2120	2360

Table 3 Relevant parameters computed from the input parameters given in Table 2. The frequency-dependent wave velocities and quality factors were all evaluated at the dominant frequency of the signal, 80 Hz.

Fig. 8 displays the inline horizontal (point) electric field E_r computed from eq. (19), the electric potential Φ given by eq. (21), the filtered electric potential Ψ_2 calculated according to eq. (22) and the voltage difference $\Delta\Phi$ obtained from the first eq. (24). The computations were performed with the model parameters listed in Table 2 for an explosive point source located at 5 m depth at the centre of the profile. We consider electric dipoles deployed at the ground surface in the direction of the profile with a spacing of 2 m between the electrodes. The source time function is a zero-phase Ricker wavelet having a dominant frequency of 80 Hz, the Nyquist frequency of the time series being 512 Hz. Among other things, the computer code of Garambois & Dietrich (2002) offers the possibility to compute partial solutions to the full medium response to emphasize some specific contributions of the wave fields. We have used this possibility in the four panels of Fig. 8 to display only the waves generated at the interface located at 35 m depth, thus excluding the direct P-wave created by the seismic source as well as the Rayleigh waves propagating along the free surface and within the first layer. In addition, the reflection coefficient of fast P-waves to EM waves has been multiplied by a factor of 10 in our simulations to amplify the weak interface response and make it more visible in our figures.

The signals presented in Fig. 8 do not show the signature of the PS wave reflection at the base of the first layer since the electric field is only sensitive to mechanical compression-dilatation motions in the $PSVTM$ wave system (Haartsen & Pride 1997). The panels only

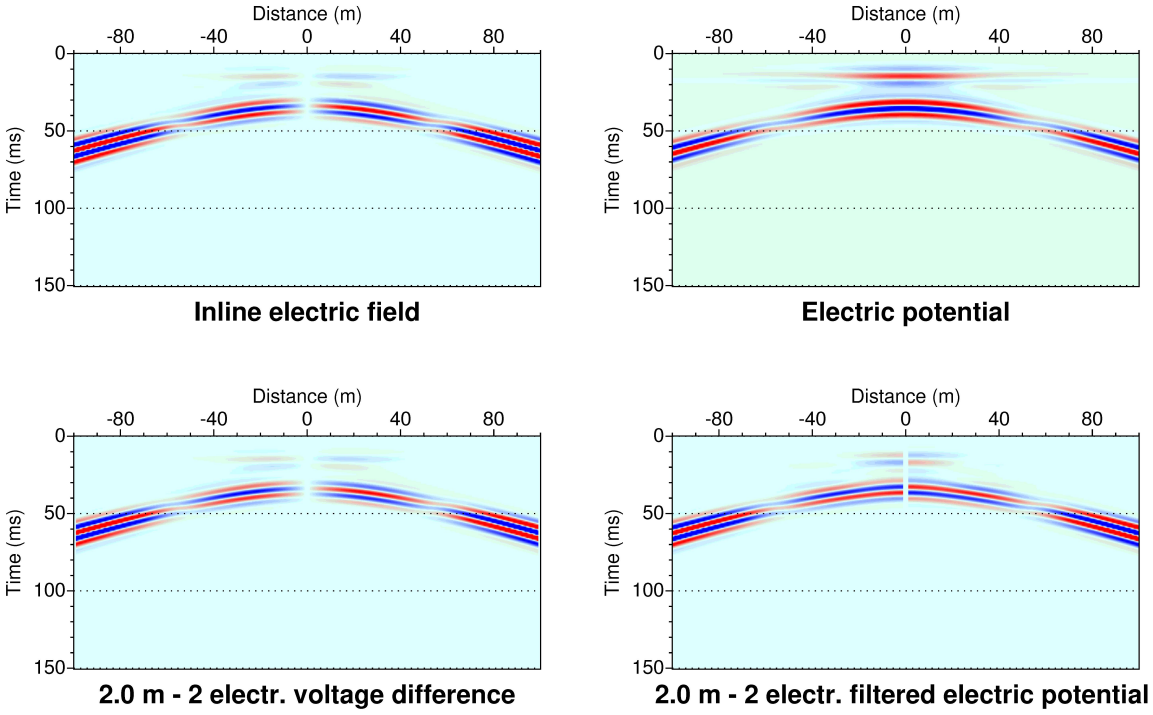

Figure 8 Electric field and electric potential sections consisting of 1001 traces spaced 0.2 m apart. The two upper panels represent the inline horizontal component of the electric field (left) and its integration over distance to obtain the electric potential (right). The two lower panels are estimates of the electric field obtained by voltage difference (left) and by implementing the filter associated with dipole measurements in the frequency-wavenumber domain (right). A dipole length of 2 m was assumed in these calculations.

show the hyperbolic PP reflection coming from the interface at 35 m depth arriving at 35 ms at zero offset. The quasi plane wave seen at small offsets around 16 ms is the interface response. The many wiggles of the reflected arrival are explained by the second derivative of the Ricker wavelet which in turn flows from the fact that the coseismic electric field is related to particle acceleration (Garambois & Dietrich 2001). The phase shift observed in the PP reflection symmetrically with respect to source position around 55 m offset corresponds to the critical distance separating pre- and post-critical reflections, where the phase of the signals rapidly changes from 0° to -180°. This critical distance is fully consistent with the critical angle of 38.45° that is readily estimated from the fast P-wave velocities given in Table 3.

The sections presented in Fig. 8 are instructive for more than one reason. Firstly, it is well observed that the inline horizontal electric field is an odd function of source-receiver offset. A more detailed analysis of the electric field waveforms would highlight the typical bell-shaped

amplitude variations of the interface response as a function of distance (Butler et al. 1996; Haartsen & Pride 1997; Beamish 1999; Garambois & Dietrich 2001). Due to integration, the electric potential is an even function of offset. The interface response has now a much clearer expression and has its maximum amplitude at zero offset. Since only voltage differences can be measured in practice, the lower left panel of Fig. 8 displays simulations of the electric field obtained from dipole measurements with a spacing of 2 m between the electrodes. A visual inspection of the voltage difference and point electric field sections enables to check the appropriateness of the former approach to estimate the electric field. The excellent match between the two solutions are shown in Fig. 9. With wavelengths on the order of 20 m for fast P-waves and 20 km for EM waves at 80 Hz, dipole measurements with an aperture of 2 m constitute indeed a very good approximation of the mathematical limit

$$E_r(r,0;t) = \lim_{d\to 0} \frac{\Delta v(r,0;t)}{d}, \quad \text{where} \quad \Delta v(r,0;t) = v\left(r-\frac{d}{2},0;t\right) - v\left(r+\frac{d}{2},0;t\right). \tag{26}$$

In this centred scheme, the electric field is evaluated in the middle of the dipoles. For that reason, some traces have been removed in the voltage difference section to account for edge effects: the missing traces lie in intervals of width $d/2$ at both ends of the profile and in a central interval of width d in the middle of the profile. In particular, it must be ensured that the two electrodes composing a dipole do not straddle the source position with one electrode in the negative offsets, and the other in the positive offsets.

This mute is also applied in the lower right panel of Fig. 8 which corresponds to the horizontal electric field evaluated from the direct inclusion of the dipole filter in the $f-k$ domain. By proceeding in this way, the coseismic part of the response is generally well reproduced, except at near offsets, but the horizontal event associated with the interface response shows significant distortions when compared to the reference electric field. The observed discrepancies are better seen in Fig. 9. They are explained by the oddness of filter $\mathcal{F}_2(k,L)$ with respect to wavenumber k, which is not properly accounted for in the axisymmetric wavenumber integration scheme used in eq. (22). This point is specifically addressed in Appendix B. In the following, we will systematically use voltage differences to simulate the electric dipole response and avoid the observed failure. The wavenumber formulation remains nevertheless very attractive for the 3- and 5-electrode arrangements and can be safely used, simply because the associated filters $\mathcal{F}_3(k,L)$ and $\mathcal{F}_5(k,L)$ are even functions of wavenumber k.

The detailed waveforms shown in Fig. 9 reinforce the observations made previously concerning the estimation of the electric field with dipoles and validity of the approaches adopted to compute voltage differences. It is seen that the coseismic PP reflection is generally well estimated at large offsets whatever the approach followed. The top row of Fig. 9 shows that

dipole measurements of voltage differences are fully consistent with the inline component of the electric field evaluated in the middle of the dipoles, at least as long as the electrode spacing remains small compared to the wavelength of the incoming signals. In this respect, the 10 m aperture of the dipole used in Fig. 9a and 9b may be considered a limiting case because it corresponds to about one half the seismic wavelength at dominant frequency. In this situation, we start observing, at relatively large offsets, minor deviations in the form of amplitude differences and small time shifts between the waveforms. The latter are induced by the time delay inherent in obliquely propagating waves when they reach the two electrodes of a dipole. As expected (but not illustrated), the agreement between electric field and voltage difference waveforms increases with decreasing dipole aperture. The significant discrepancies that are manifest at small offsets in Fig. 9c and 9e, and to a lesser extent at large offsets in Fig. 9d and 9f when comparing voltage differences with the filtering performed internally in the simulation code are solely due to the limitations of the wavenumber integration technique, as outlined above.

The overall remark that can be made from Fig. 8 and 9 is that dipole measurements perform poorly when it comes to record the interface response. The latter would be much better detected if it were possible to measure the electric potential rather than the electric field, as already suggested. This result can be achieved to a good degree of efficiency by considering the 3-electrode linear voltage combinations introduced in Fig. 3b and eq. (10). Their relevance is demonstrated with full waveform numerical simulations in Fig. 10. The two sections in the bottom row first demonstrate the equivalence of the two alternative solutions given in eq. (24) to compute the combinations of electric potential. More importantly, it is seen that the resulting signals reproduce quite well the electric potential signals displayed in the upper right panel, therefore providing a numerical proof of eq. (10). However, a closer look at the waveforms presented in Fig. 11 reveals some discrepancies for the PP reflection at large offset (Fig. 11b), which is explained by the obliquity of its wavefront. In this case indeed, the approximation made in the right-hand side of eq. (10) breaks down because it is only strictly valid for a plane wave arriving parallel to the ground surface with uniform amplitude distribution. As a matter of fact, the $(+ - +)$ averaging of electric potential works well for the interface response which appears to be virtually identical to its electric potential. Fig. 11c, 11d, 11e and 11f simply show that the two approaches advocated for implementing the filtering effects of electrode arrays in numerical simulations, the 'inner' and 'outer' techniques presented in eq. (24), are here in very good agreement.

To conclude this discussion and evaluate the benefit of using 3-electrode arrays rather than

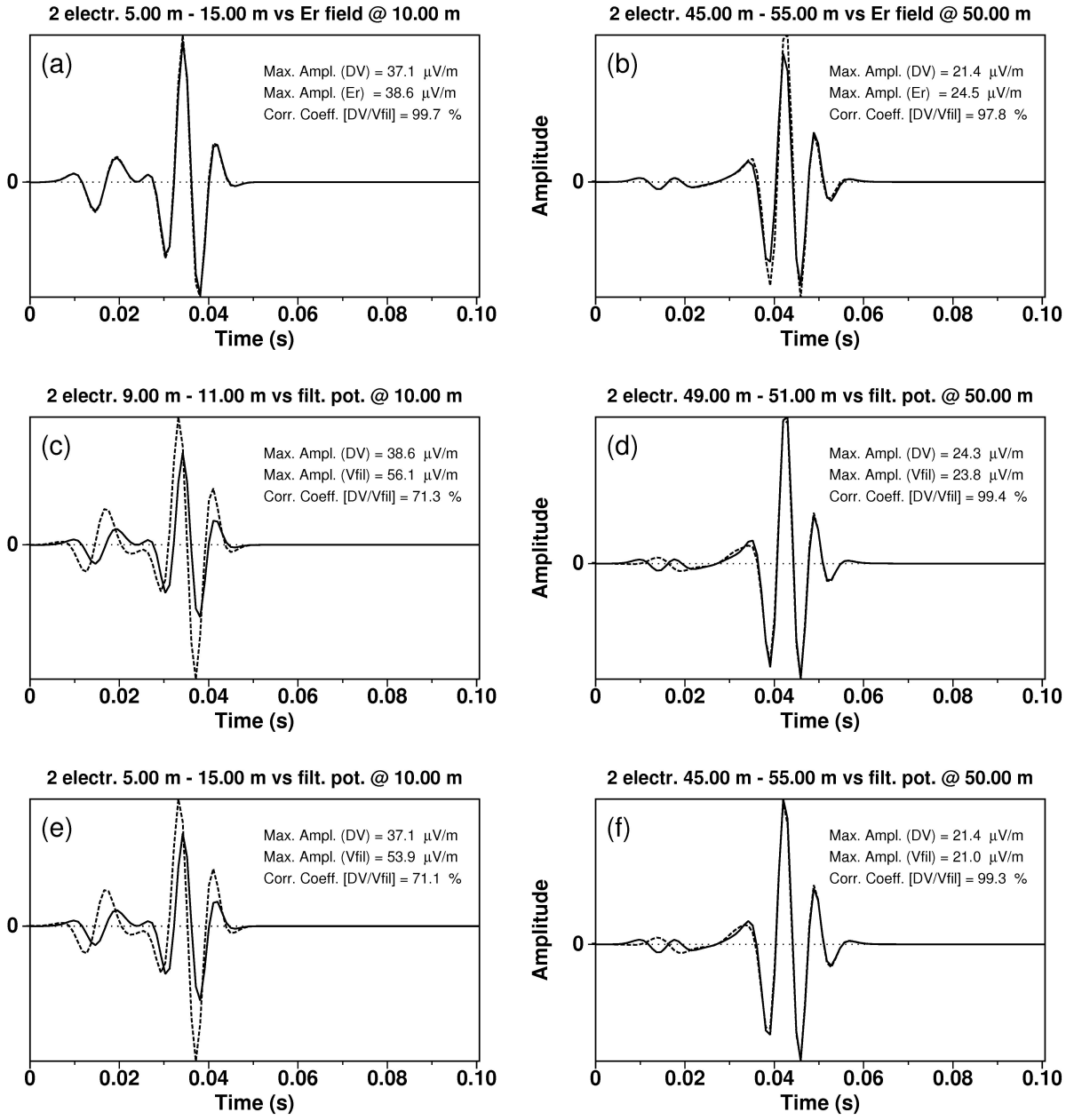

Figure 9 Electric field measurements with dipoles. The left-hand and right-hand columns respectively display comparisons made at 10 m and 50 m source-receiver offsets. The two panels in the top row compare voltage differences (noted *DV*, solid lines) with the electric field computed in the middle of 10 m long dipoles (noted *Er*, dashed lines). The middle and bottom rows show comparisons between voltage differences computed at ground surface (*DV*, solid lines) and electric field obtained from the filtered potential in the $f - k$ domain (noted *Vfil*, dashed lines) by simulating dipoles with lengths of 2 m and 10 m. The maximum amplitudes and correlation coefficient of the two signals are indicated in each box.

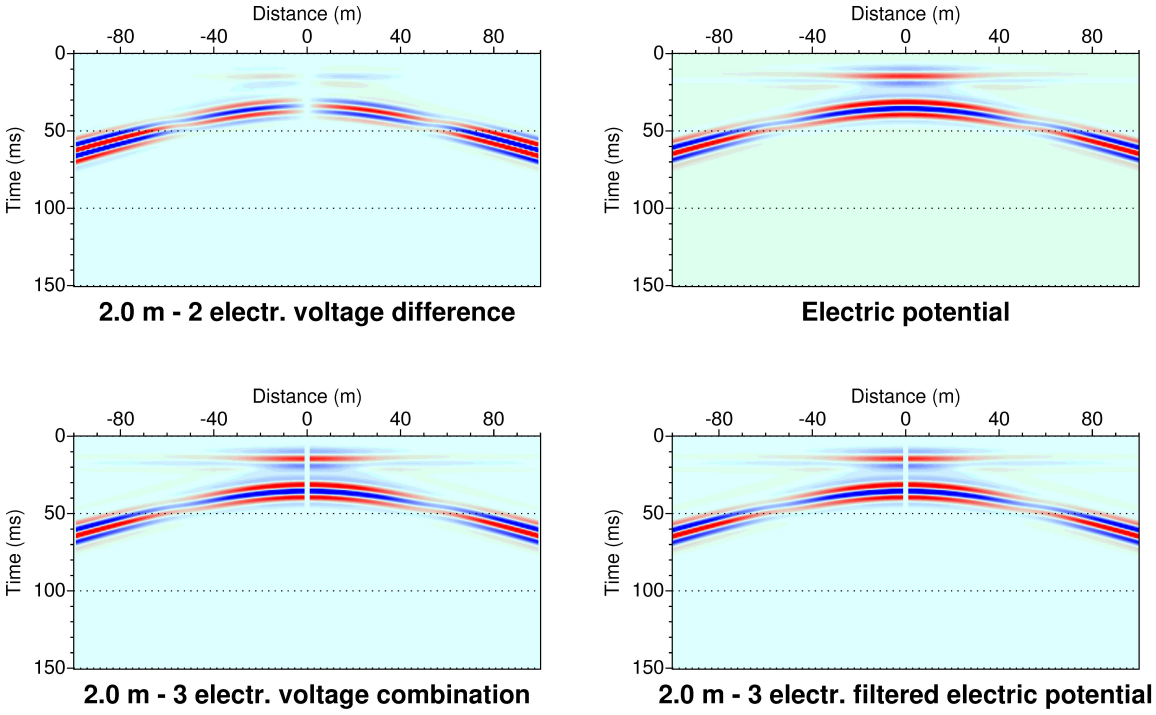

Figure 10 Electric field and electric potential sections obtained with the same model and computation parameters as in Fig. 8. The two upper panels reproduce, for comparison, the electric potential signals (right) and the derived dipole records (left) already shown in Fig. 8. The two lower panels display combinations of 3 electric potentials simulating the 3-electrode arrangement shown in Fig. 3b. The combinations are performed both in the time-distance domain from the computed voltage signals (left) and by directly implementing the filter in the frequency-wavenumber domain (right). An electrode array length of 2 m was assumed in all these calculations.

electric dipoles in seismoelectric measurements, we present in Fig. 12 the amplitude versus offset (AVO) variations of the two events composing the synthetic traces displayed in Fig. 8 to 11, i.e., the interface response on the one hand and the coseismic PP reflection on the other hand. Fig. 12a and 12b show the absolute RMS amplitudes of these two arrivals computed with their correct magnitude (without amplifying the interface response) for positive source-receiver offsets and four different situations: dipole and 3-electrode recordings, and for each of them, 2 and 10 m array lengths. The kink that is visible on the PP reflection curves around 55 m offset (Fig. 12a) is associated with the critical distance already identified in Fig. 8. Broadly speaking, the AVO curves of Fig. 12a mimic the amplitude versus angle behaviour of the PP reflection coefficient. The tapering that is manifest at near offsets for the dipole measurements

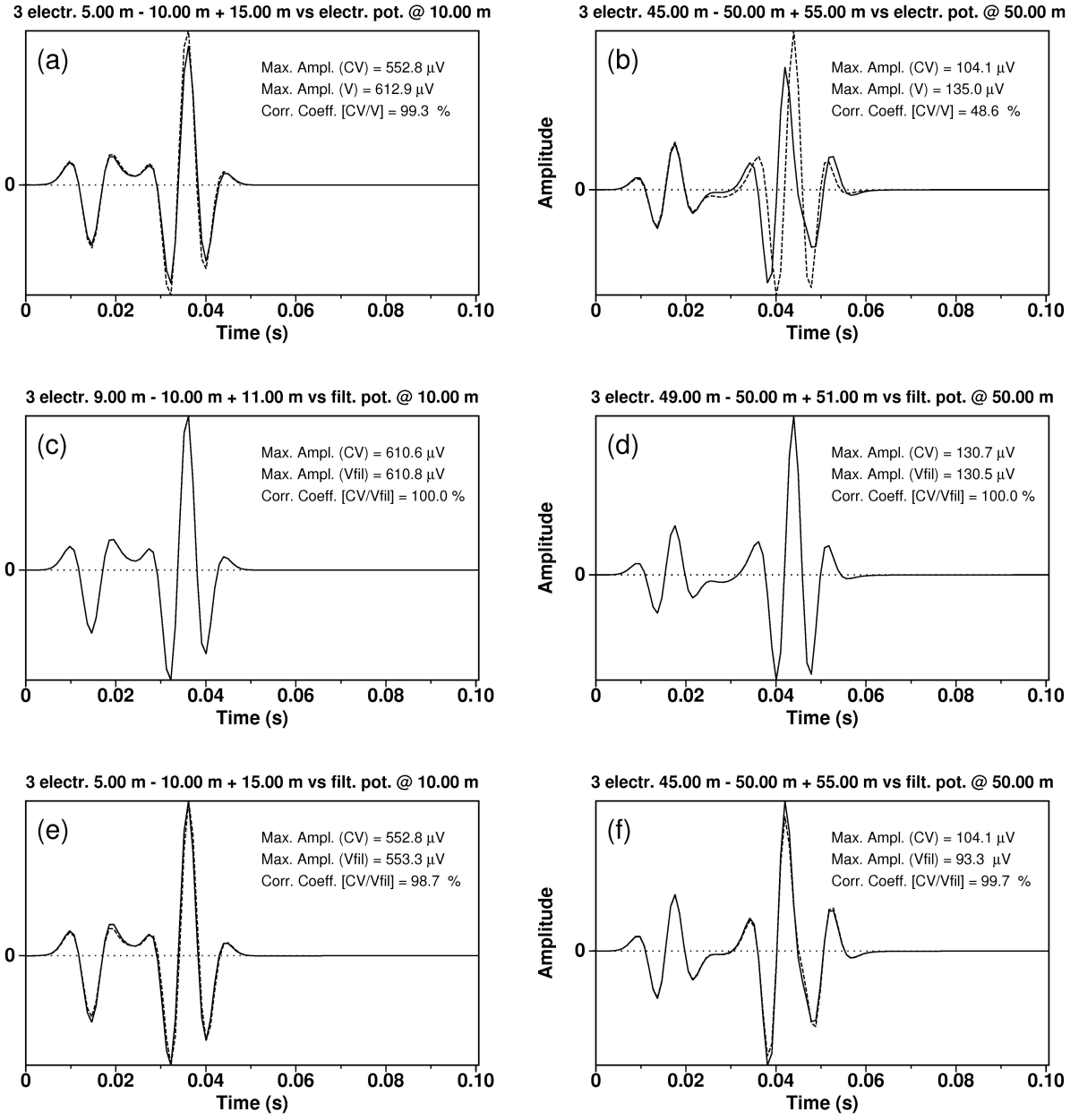

Figure 11 Electric measurements with 3-electrode arrangements. The left-hand and right-hand columns respectively display comparisons made at 10 m and 50 m source-receiver offsets. The two panels in the top row compare the 3-electrode voltage combinations (noted CV, solid lines) with the electric potential computed in the middle of 10 m long electrode arrangements (noted V, dashed lines). The middle and bottom rows show comparisons between voltage combinations computed at ground surface (CV, solid lines) and electric signals obtained from the filtered potential in the $f - k$ domain (noted *Vfil*, dashed lines) by simulating electrode arrays with lengths of 2 m and 10 m. The maximum amplitudes and correlation coefficient of the two signals are indicated in each box.

is due to the fact that the dipole filter is an odd function of offset. By contrast, the 3-electrode filter response is an even function of offset and is perfectly symmetric with respect to the zero-offset axis. Evenness and oddness also characterize the 3-electrode and dipole simulations of the interface response (Fig. 12b) with an obvious advantage for the 3-electrode configuration at near offsets, reflected by a strong amplification of the signal, especially between 0 and 15 m offset. The almost perfect coincidence of the AVO curves associated with the 2 m and 10 m long 3-electrode arrays is fully consistent with previous observations indicating that such configurations accurately measure the electric potential of plane waves propagating parallel to the ground surface. The dipole measurements are much more sensitive to the electrode spacing. They reproduce the typical bell-shape amplitude radiation of a virtual dipole located on the reflector at 35 m depth right below the source location. Finally, Fig. 12c presents the variations of the amplitude ratio between the interface response and the coseismic PP reflection as a function of offset for the four situations considered. Fig. 12c shows again the superiority of the 3-electrode array for the detectability of the precursory EM wave arrival, at least beyond an offset of 20 m. At short offets, multi-electrode arrays also enhance the quasi-horizontal plane wave components of the hyperbolic PP reflection near its apex. While this may seem somewhat disappointing, it must be underlined that in real situations, near-surface reflections are usually hidden behind the much stronger direct and surface waves which propagate horizontally with vertical wavefronts.

We end this section on numerical simulations by considering in Fig. 13 a 6-layer model constructed from the properties given in Table 1, by alternating layer 1 and layer 2 with interfaces located at 3.5, 5, 8, 20 and 50 m depth. Starting with the properties of layer 1 near the surface, the stratification ends with a lower half space having the properties of layer 2. The explosive point source is at 2 m depth. Our computations simulate the full waveform responses of 2 m long electric dipoles and 3-electrode arrays of the same length. The modelled waveforms include all contributions to the wave fields, i.e., direct, surface and interface waves as well as all multiple reflections and mode-converted waves, and near-field effects. The interface responses are calculated with their true magnitudes, i.e., without artificially amplifying the P to EM reflection coefficients, to conform to real situations.

As expected with the model considered, the 2-electrode voltage difference section (upper left panel) is strongly dominated by the electrical signature of dispersive Rayleigh waves. The latter often represent the most energetic contribution to seismic field records. It turns out that the seismoelectric counterparts of surface waves are further favoured by the filtering effects of electric dipoles which attenuate the plane-wave components arriving more or less

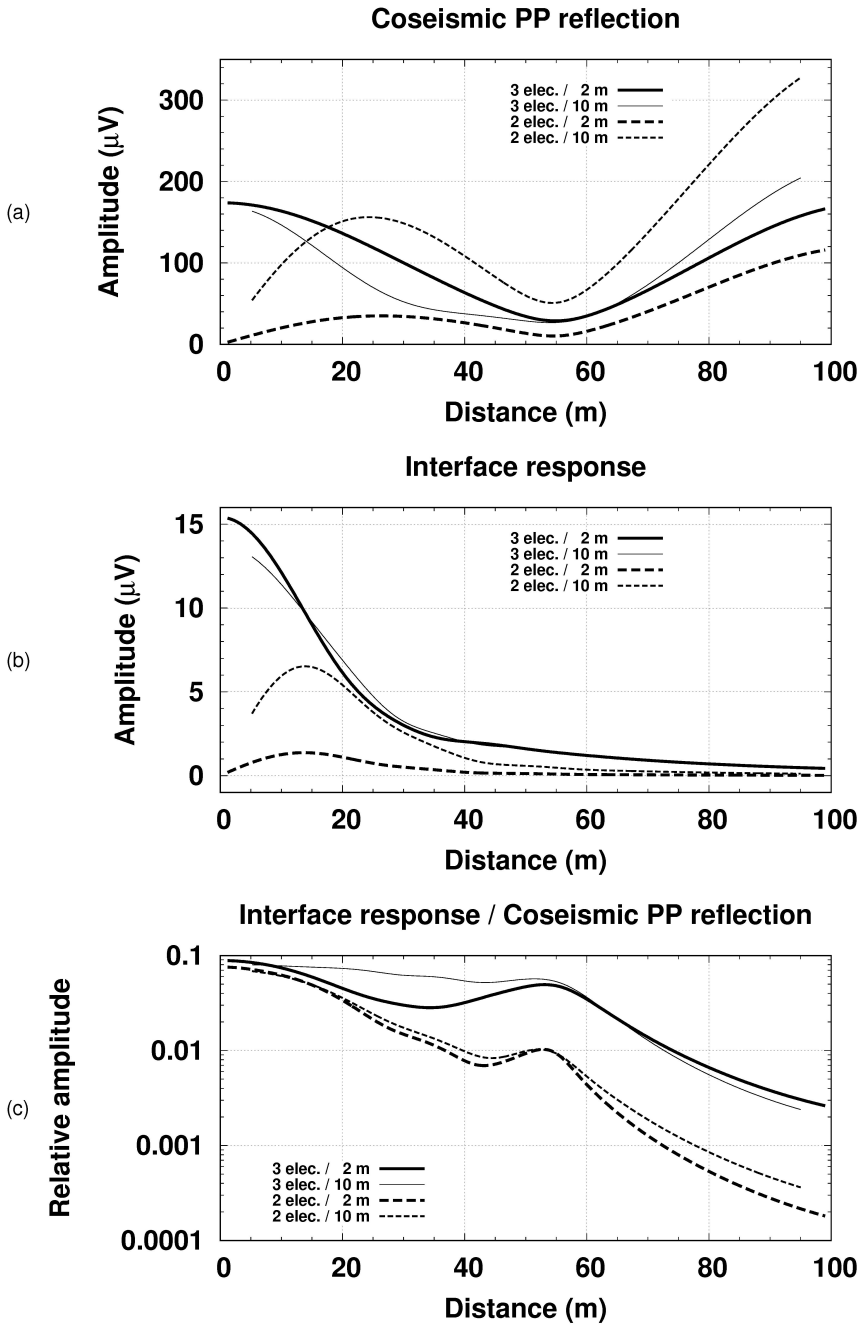

Figure 12 Amplitude versus offset (AVO) curves of electric signals obtained by simulating data acquisition with dipoles and 3-electrode arrays. The model used for the computations is the same as in Fig. 8-11. The interface response is computed with its true amplitude, without amplification. The voltage difference traces of Fig. 8 and voltage combination traces of Fig. 10 have been split in two parts: the early part (0-25 ms) representing the interface response and the subsequent arrival (25-80 ms) consisting of the coseismic PP reflection. Panels (a) and (b) display the AVO curves of the coseismic PP reflection and interface response respectively, for the two array types and two array lengths. Panel (c) displays the amplitude ratios between the interface response and coseismic PP reflection in the four situations considered.

parallel to the ground surface and therefore reinforce all other components. This observation is consistent with our previous analytical developments and is clearly evidenced by comparing the electric dipole section (upper left panel) with the electric voltage section (upper right panel) and with the 3-electrode voltage combination section (lower left section). It is seen that low wavenumber arrivals are much better preserved in the electric voltage and 3-electrode array sections. Both of them display some hints of interface responses in the early part of the sections. In appearence, the 3-electrode array response gives even better results than the electric potential when it comes to reproduce horizontal plane waves. This fact is simply explained by the tuning operated by the 3-electrode arrays in favour of vertically propagating plane waves, at the expense of plane waves propagating obliquely relative to the ground surface. Compared to the electric potential section, it is indeed observed that the seemingly better performance of the 3-electrode arrays to preserve the horizontal plane waves comes with a degraded signature of the strongly dipping events associated with the surface waves.

Finally, the lower right panel of Fig. 13 confirms once again the superiority of the multi-electrode approach for detecting EM interface responses. These arrivals are virtually invisible in the early part of the electric dipole section but can clearly be seen on the 3-electrode array response. The theoretical arrival times of the EM disturbances generated at the 5 interfaces of the model are 0.8, 1.3, 2.9, 6.9 and 23.1 ms as primary reflections. Additional EM contributions related to multiple reflections and mode-converted waves, and the overlapping with coseismic reflections blur the detailed interpretation of the observed events.

Fig. 14 gives quantitative estimates of the amplitude ratio between the interfaces responses and coseismic events found in the time intervals 0–18 ms and 18–150 ms for the realistic 6-layer simulation used in Fig. 13. The chosen time intervals include the $P-EM$ conversions at the four uppermost reflectors. The amplitudes are analyzed in the offset range 25–99 m which is mainly outside of the so-called 'noise cone' (direct and guided waves). Between 25 m and 60 m offset, the 2 m long 3-electrode array are shown to be up to 14 times more efficient than its dipole counterpart in terms of amplitude ratio between the the interfaces responses and coseismic events. Larger offsets are less relevant because of the vanishingly small amplitudes of the interface responses.

5 CONCLUSIONS

In seismoelectric surveys, the transient electric field generated by seismic vibrations cannot strictly be measured at a point. The horizontal component of the electric field is conventionally estimated from the gradient of the electric potential across two grounded and closely spaced

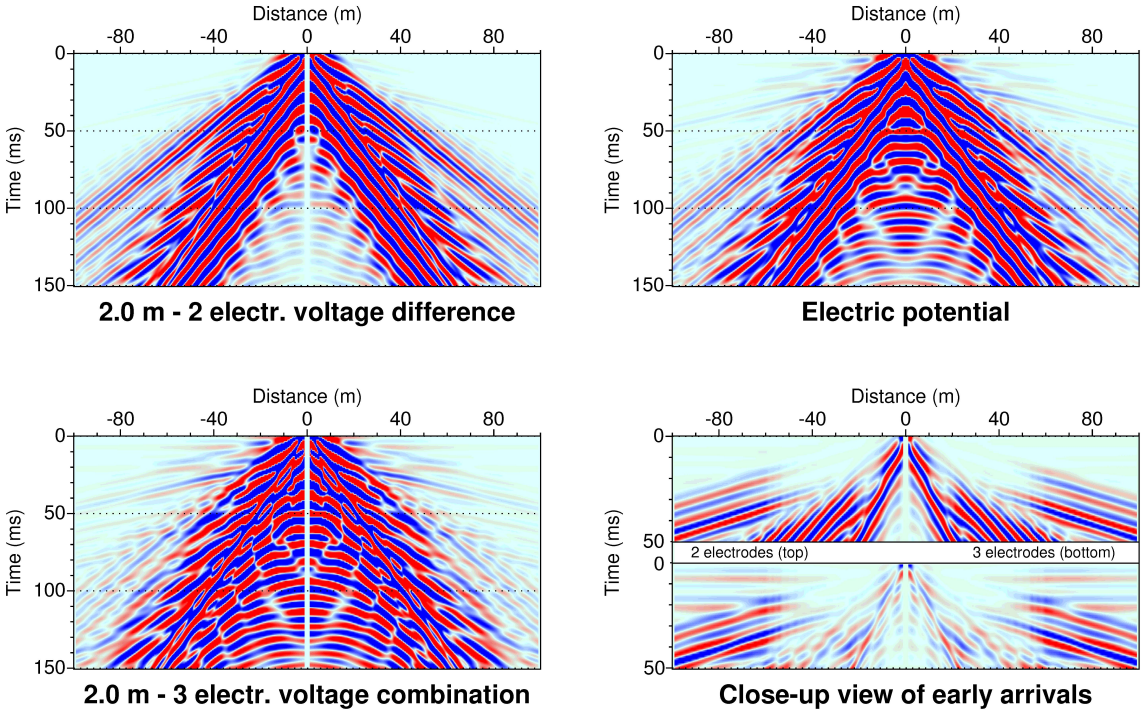

Figure 13 Electric dipole and 3-electrode array responses computed for a 6-layer model and electrode array lengths of 2 m. The upper right panel displays the electric potential signals. The upper left panel shows the derived dipole records. The lower left panel displays signals simulating the 3-electrode arrangement shown in Fig. 3b. The amplitudes are clipped relative to their maximum value in each of these three panels. The lower right panel displays the early part of the dipole and 3-electrode sections. A trace-by-trace normalization was used in this plot. Additionally, the amplitudes of the dipole traces were uniformly amplified by a factor 1.5 so that the P-wave reflections show up with similar amplitudes in the two sections.

electrodes. While being mathematically correct, this approach entails some drawbacks that we have investigated in detail in this study. An electric dipole measuring a voltage difference behaves like an array of two receivers whose filtering properties must be accounted for, or at least kept in mind, in seismoelectric data acquisition, processing and interpretation. Our investigations show that electric dipoles are inherently characterized by a band-pass filter as a function of horizontal wavenumber, with detrimental effects at low frequencies for wave field components arriving exactly or nearly parallel to the ground surface. The only leeway for tuning electric dipoles is to vary the spacing between the two electrodes. In practice, this can only be done within certain limits, on the one hand because the search for a suitable signal-to-noise ratio requires a minimum electrode separation, and on the other hand because large

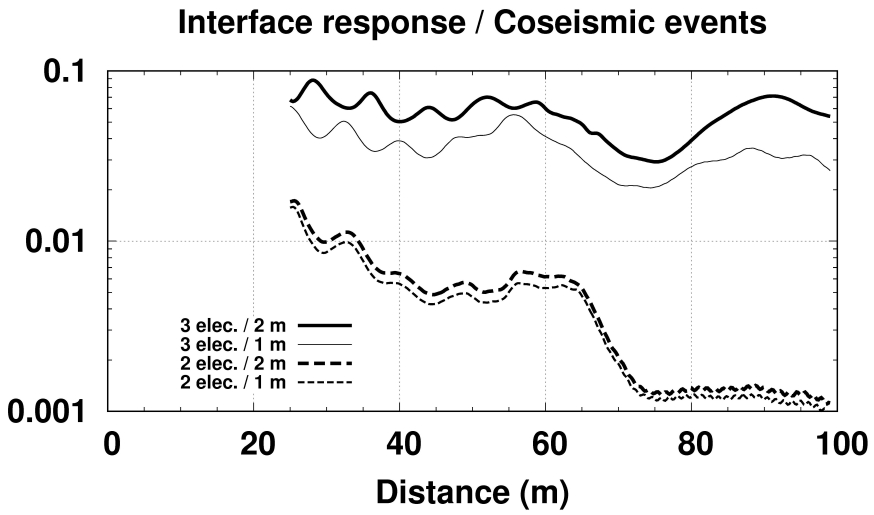

Figure 14 Amplitude ratios between the interface responses and coseismic PP reflections as a function of offset for signals simulating 1 m and 2 m long dipoles and 3-electrode arrays in the 6-layer model.

electrode spacings lead to unwanted wave field averaging. It turns out that, in field surveys, electric dipoles do not permit to preserve the various components of seismoelectric wave fields, except the surface waves to a certain extent. A compensation of the filtering effects via signal processing appears just as illusory as it would require a delicate plane wave decomposition of the recorded wave fields (see, e.g., Dietrich 1990) prior to an equally difficult deconvolution of the plane wave components thus obtained.

The main idea developed in this paper is to replace the conventional measurement of voltage difference by another measure also based on a voltage difference but one that involves an odd number of electrodes connected together via a specific $(+-+)$ pattern. We have demonstrated, both analytically and numerically, that the proposed electrode arrangements make it possible to obtain estimates of the electric potential rather than the electric field for horizontal plane waves, and therefore permit to remove most of the unwanted filtering effects of electric dipoles. The wavenumber filters representing these multi-electrode arrangements are low-pass filters which are essentially capable of retaining the interface response arrivals, recognized as the weakest but also the most valuable contributions to seismoelectric measurements. The minimum configuration involves three equidistant electrodes where the two outside electrodes are connected together, the voltage difference being taken with respect to the centre electrode. Arrangements involving a larger number of equidistant electrodes have the potential to reach higher filter gains in specific frequency ranges.

The practical implementation of such configurations requires only slight modifications of the data acquisition scheme and electrode wiring. It involves only additions and subtractions of electric potential which are perfectly stable operations unlike deconvolution algorithms which rely on divisions. However, the efficiency of this approach can be substantially challenged by an inaccurate, non-equidistant, electrode placement or by an irregular weighting of the electrodes resulting from poor ground coupling. All these aspects are likely to deteriorate the performance of multi-electrode arrays, and in the worst cases, to cancel out completely their benefits. This calls for due attention during the installation of the electrodes. With this reservation, improvements are expected over conventional electric measurements, most likely at a lower level than predicted by the theory, but significant enough to warrant the use of multi-electrode arrays in seismoelectric surveys. The filtering properties of electric dipoles and multi-electrode arrays are further investigated in the context of laboratory experiments in our companion paper (Devi et al. 2018).

The developments presented in this work were first obtained analytically by using a filter theory approach restricted to incident plane waves. Our results were then confirmed and consolidated by means of numerical simulations dealing with the full complexity of the coupled seismic and electromagnetic wave propagation in fluid-filled porous media, however without adding harmonic noise for enhanced realism. This second approach has required the derivation and computation of the electric potential from the electric field. We have also shown that the formulation used for the forward modelling makes it possible to directly include the filtering effects of electrode arrangements in the course of the computations. The quantitative estimates of the electric potential and electrode array responses will be necessary ingredients in a full waveform inversion of seismoelectric data yet to come.

Finally, the multi-electrode approach advocated in this work could easily be adapted for beam steering purposes by moving, for instance, the central electrode of a 3-electrode array towards one or the other of the two outer electrodes in order to favour oblique events with positive or negative slopes. Another possible extension of the proposed theory is a cascaded application of the 3- or 5-electrode filters to further enhance the interface responses. Such a scheme would simply consider the filtered interfacial events directly obtained in field measurements as electric potentials ready to be recombined, via post-processing, according to a 3- or 5-electrode configuration. This operation can possibly be repeated many times to preserve zero-wavenumber events while attenuating all other arrivals to varying degrees. Areal (2D) deployments of electrodes remain to be investigated for this objective.

ACKNOWLEDGMENTS

This work has been supported by a grant from LabEx OSUG@2020 (Investissements d'Avenir - ANR10 LABX56) and by a doctoral scholarship awarded by the French Ministry of Higher Education and Research. We thank Glenn Cougoulat for useful technical discussions in the course of this work and the reviewers for their constructive comments.

REFERENCES

REFERENCES

Abramowitz, M. & Stegun, I. A., 1964. *Handbook of mathematical functions with formulas, graphs, and mathematical tables*, National Bureau of Standards Applied Mathematic Series.

Beamish, D., 1999. Characteristics of near-surface electrokinetic coupling, *Geophysical Journal International*, **137**, 231–243.

Bouchon, M., 1979. Discrete wave number representation of elastic wave fields in three-space dimensions, *Journal of Geophysical Research*, **84**, 3609–3614.

Bouchon, M., 1981. A simple method to calculate greens functions for elastic layered media, *Bulletin of the Seismological Society of America*, **71**, 959–971.

Butler, K. E. & Russell, R. D., 1993. Subtraction of powerline harmonics from geophysical records, *Geophysics*, **58**(6), 889–903.

Butler, K. E., Russell, R. D., Kepic, A. W., & Maxwell, M., 1996. Measurement of the seismoelectric response from a shallow boundary, *Geophysics*, **61**(6), 1769–1778.

Butler, K. E., Kulessa, B., & Pugin, A., 2018. Multimode seismoelectric phenomena generated using explosive and vibroseis sources, *Geophysical Journal International*, **213**(2), 836–850.

Devi, M. S., Garambois, S., Brito, D., Dietrich, M., Poydenot, V., & Bordes, C., 2018. A novel approach for seismo-electric measurements using multi-electrode arrangements: Ii - laboratory measurements, *Geophysical Journal International*, **214**(3), 1783–1799.

Dietrich, M., 1990. An algorithm for the plane-wave decomposition of point-source seismograms, *Geophysics*, **55**(10), 1380–1385.

Dupuis, J. C., Butler, K. E., & Kepic, A. W., 2007. Seismoelectric imaging of the vadose zone of a sand aquifer, *Geophysics*, **72**(6), A81–A85.

Garambois, S. & Dietrich, M., 2001. Seismoelectric wave conversions in porous media: Field measurements and transfer function analysis, *Geophysics*, **66**(5), 1417 – 1430.

Garambois, S. & Dietrich, M., 2002. Full waveform numerical simulations of seismo-electromagnetic wave conversions in fluid-saturated porous media, *Journal of Geophysical Research*, **107**(B7), ESE 5–1 – ESE 5–18.

Haartsen, M. W. & Pride, S., 1997. Electroseismic waves from point sources in layered media, *Journal of Geophysical Research*, **102**(24), 745 – 769.

Hornbostel, S. & Thompson, A. H., 2007. Waveform design for electroseismic exploration, *Geophysics*, **72**(2), Q1–Q10.

Johnson, C. H., 1939. Steady state polar sensitivity curves, *Geophysics*, **4**(1), 33–52.

Kennett, B. L. N., 1983. *Seismic Wave Propagation in Stratified Media*, Cambridge UNiversity Press.

Lombardi, L. V., 1955. Notes on the use of multiple geophones, *Geophysics*, **20**(2), 215–226.

Luke, Y. L., 1975. *Mathematical functions and their approximations*, Academic Press.

Martner, S. T. & Sparks, N. R., 1959. The electroseismic effect, *Geophysics*, **24**(2), 297–308.

Mikhailov, O. V., Haartsen, M. W., & Toksoz, M. N., 1997. Electroseismic investigation of the shallow subsurface: Field measurements and numerical modeling, *Geophysics*, **62**(1), 97–105.

Pride, S., 1994. Governing equations for the coupled electromagnetics and acoustics of porous media, *Physical Review B Condensed Matter*, **50**(21), 15678–15696.

Pride, S. & Haartsen, M. W., 1996. Electroseismic wave properties, *Journal of the Acoustical Society of America*, **100**(3), 1301–1315.

Ren, H., Huang, Q., & Chen, X., 2015. Existence of evanescent electromagnetic waves resulting from seismoelectric conversion at a solidporous interface, *Geophysical Journal International*, **204**, 147–166.

Revil, A., Jardani, A., Sava, P., & Haas, A., 2015. *The Seismoelectric Method: Theory and Application*, John Wiley and Sons.

Thompson, A. H. & Gist, G. A., 1993. Geophysical applications of electrokinetic conversion, *The Leading Edge*, **12**, 1169–1173.

Thompson, A. H., Hornbostel, S., Burns, J., Murray, T., Raschke, R., Wride, J., McCammon, P., Sumner, J., Haake, G., Bixby, M., Ross, W., White, B. S., Zhou, M., & Peczak, P., 2007. Field tests of electroseismic hydrocarbon detection, geophysics, *Geophysics*, **72**(1), N1–N9.

Thompson, R. R., 1936. The seismic electric effect, *Geophysics*, **1**, 327–335.

Vermeer, G. J. O., 2002. *3-D seismic survey design*, vol. 12 of **Geophysical references series**, Society of Exploration Geophysicists.

Zhu, Z., Haartsen, M. W., & Toksoz, M. N., 2000. Experimental studies of seismoelectric conversions in fluid-saturated porous media, *Journal of Geophysical Research*, **105**(B12), 2805528064.

Zonge, K. L. & Hughes, L. J., 1985. The effect of electrode contact resistance on electric field measurements, *55th Annual SEG Convention, Washington, D.C., October 6-10*.

APPENDIX A: MULTI-ELECTRODE FILTER RESPONSES

We derive in this section some of the equations presented in the main text and provide additional details and proofs for some of the results.

A1 Electric dipoles

The frequency range $[f_1, f_1']$ in which signals are amplified with amplitudes greater than 1 is determined by the following condition derived from eq. (6)

$$|\, G_{2el}(f_1)\,| = 2\,|\sin(\pi\tau f_1)| = 1, \tag{A.1}$$

where f_1 denotes the lower end of the frequency range requested. The upper end f_1' is given by the same equation. For positive frequencies, this equation implies that $\pi\tau f_1 = \arcsin(1/2)$ whose values are $\{\pi/6, 5\pi/6\}$. Hence,

$$\{f_1, f_1'\} = \left\{\frac{1}{6\tau}, \frac{5}{6\tau}\right\}. \tag{A.2}$$

A2 3- and 5-electrode arrays

To demonstrate the first equality on the right-hand side of eq. (12), we write eq. (10) in the Fourier domain, i.e.,

$$S_{3el}(f) = \vartheta_1(f)\, G_{3el}(f), \quad \text{where} \quad G_{3el}(f) = 1 - e^{-i\pi\tau f} + e^{-i2\pi\tau f}. \tag{A.3}$$

Expressing $G_{3el}(f)$ as $e^{-i\pi\tau f}\left[e^{i\pi\tau f} - 1 + e^{-i\pi\tau f}\right]$, we get

$$G_{3el}(f) = e^{-i\pi\tau f}\,[2\cos(\pi\tau f) - 1] \quad \text{and} \quad |G_{3el}(f)| = |2\cos(\pi\tau f) - 1|\,. \tag{A.4}$$

Similarly, for 5-electrode configurations,

$$G_{5el}(f) = 1 - e^{-i\pi\tau f/2} + e^{-i\pi\tau f} - e^{-i3\pi\tau f/2} + e^{-i2\pi\tau f}. \tag{A.5}$$

Factorizing again $\exp(-i\pi\tau f)$, we obtain

$$G_{5el}(f) = e^{-i\pi\tau f}\left[e^{i\pi\tau f} - e^{i\pi\tau f/2} + 1 - e^{-i\pi\tau f/2} + e^{-i\pi\tau f}\right], \text{ that is,}$$

$$\begin{aligned} G_{5el}(f) &= e^{-i\pi\tau f}\,[2\cos(\pi\tau f) - 2\cos(\pi\tau f/2) + 1], \text{ and} \\ |G_{5el}(f)| &= |2\cos(\pi\tau f) - 2\cos(\pi\tau f/2) + 1|\,. \end{aligned} \tag{A.6}$$

Using the trigonometric identity $\cos 2\theta = 2\cos^2\theta - 1$, the above expression can alternatively be written as

$$|G_{5el}(f)| = \left|4\cos^2(\pi\tau f/2) - 2\cos(\pi\tau f/2) - 1\right|. \tag{A.7}$$

A3 General case: N-electrode arrays

The general case of an electrode array consisting of an odd number N of electrodes is treated by extending the scheme depicted in Fig. 3b and 3c as well as the previous equations. We consider as before an array of fixed length L subdivided into $N-1$ intervals. τ is the total

delay time of the incoming plane wave between the first and last electrodes of the array. The corresponding transfer function $G_{Nel}(f)$ writes

$$G_{Nel}(f) = 1 - \exp\left(\frac{-i2\pi\tau f}{N-1}\right) + \exp\left(\frac{-i4\pi\tau f}{N-1}\right) - \exp\left(\frac{-i6\pi\tau f}{N-1}\right) \cdots + \exp\left(-i2\pi\tau f\right) \quad \text{(A.8)}$$

Shifting the above N-term series by one time delay increment and adding the result to the original sequence leads to the following compact result

$$G_{Nel}(f) + G_{Nel}(f)\,\exp\left(\frac{-i2\pi\tau f}{N-1}\right) = 1 + \exp\left(\frac{-i2N\pi\tau f}{N-1}\right)$$

from which we infer that

$$G_{Nel}(f) = \frac{1 + \exp\left(\frac{-i2N\pi\tau f}{N-1}\right)}{1 + \exp\left(\frac{-i2\pi\tau f}{N-1}\right)} = \frac{\exp\left(-i\pi\tau f\frac{N}{N-1}\right)\,\cos\left(\pi\tau f\frac{N}{N-1}\right)}{\exp\left(-i\pi\tau f\frac{1}{N-1}\right)\,\cos\left(\pi\tau f\frac{1}{N-1}\right)}. \quad \text{(A.9)}$$

Consequently,

$$|G_{Nel}(f)| = \left|\frac{\cos\left(\pi\tau f\,\frac{N}{N-1}\right)}{\cos\left(\pi\tau f\,\frac{1}{N-1}\right)}\right|. \quad \text{(A.10)}$$

The zeroes of the numerator are determined by

$$\pi\tau f_{0m}^{[num]}\,\frac{N}{N-1} = \frac{\pi}{2} + m\pi,\ m = 0, 1, 2, \ldots, \text{ implying that } f_{0m}^{[num]} = \frac{N-1}{2N\tau}\,(1+2m)\,. \quad \text{(A.11)}$$

The zeroes of the denominator are similarly given by

$$f_{0m'}^{[den]} = \frac{N-1}{2\tau}\,\left(1+2m'\right),\ m' = 0, 1, 2, \ldots. \quad \text{(A.12)}$$

The filter response is cancelled whenever the numerator is equal to zero, except when the denominator is also equal to zero. This happens when the two nulling frequencies $f_{0m}^{[num]}$ and $f_{0m'}^{[den]}$ coincide, which corresponds to the condition $m = (N-1)/2 + Nm'$. In practice, it suffices to consider the nulling frequencies $f_{0m'}^{[den]}$ which are multiples of the frequencies $f_{0m}^{[num]}$. In such cases, the indeterminate form can be resolved by using L'Hôpital's rule, i.e., by evaluating the derivatives of the numerator and denominator with respect to frequency at the specific nulling frequencies $f_{0m'}^{[den]}$, namely,

$$\begin{aligned}
\lim_{f \to f_{0m'}^{[den]}} |G_{Nel}(f)| &= \left|\frac{-\pi\tau\frac{N}{N-1}\,\sin\left(\pi\tau f\,\frac{N}{N-1}\right)}{-\pi\tau\frac{1}{N-1}\,\sin\left(\pi\tau f\,\frac{1}{N-1}\right)}\right|_{f=f_{0m'}^{[den]}} \\
&= N\left|\frac{\sin\left(\pi\tau f\,\frac{N}{N-1}\right)}{\sin\left(\pi\tau f\,\frac{1}{N-1}\right)}\right|_{f=f_{0m'}^{[den]}} \quad \text{(A.13)}
\end{aligned}$$

Starting with the low frequencies, the first and second occurences of the indeterminate form are from eq. (A.12),

$$f_{00}^{[den]} \equiv f_{max_1} = \frac{N-1}{2\tau} \quad \text{and} \quad f_{01}^{[den]} \equiv f_{max_2} = \frac{3(N-1)}{2\tau} \tag{A.14}$$

Setting for instance $f = f_{max_1}$ in eq. (A.13) then yields

$$|G_{Nel}(f_{max})| = N \left| \frac{\sin(N\pi/2)}{\sin(\pi/2)} \right| = N \quad \text{since } N \text{ is an odd integer by definition.} \tag{A.15}$$

We have thus demonstrated that the frequency response of an electrode array comprising an odd number N of equidistant, non-weighted electrodes alternatively connected with positive and negative polarities has a maximum absolute amplitude N. This maximum amplitude is associated with the zeroes of the denominator of $|G_{Nel}(f)|$ (eq. A.10) whereas the notches of the filter are determined by the zeroes of its numerator. For 3-electrode arrays, the zeroes are given by $f_{0m} = (1+2m)/3\tau$, that is, $\{1/3\tau, 5/3\tau, 7/3\tau, \ldots\}$, where we have notably skipped the value $3/3\tau$ which is f_{max_1} for that configuration. The maximum amplitude is reached the second time for $f_{max_2} = 3/\tau$. For 5-electrode arrays, the zeroes are given by $f_{0m} = (2+4m)/5\tau$, that is, $\{2/5\tau, 6/5\tau, 14/5\tau, \ldots\}$, where we have skipped the value $10/5\tau$ which is f_{max_1} for that configuration. The maximum amplitude is reached the second time for $f_{max_2} = 6/\tau$. These properties are illustrated in Fig. 4 and summarized in Table 1.

APPENDIX B: DIRECT MODELLING OF THE FILTER RESPONSE

In this section, we give explanations as to why the direct implementation of the dipole filter within the frequency - wavenumber loop of our modelling programme fails to provide the correct response for wavefronts arriving more or less parallel to the ground surface.

Fig. B.1 illustrates the construction of a circular wavefront originating from a seismic point source by a summation of plane waves of different wavenumbers (or inclinations). It schematically describes the wavenumber integrations of eq. (19), (21) and (22) which are much more general in their scope. Fig. B.1 shows that because of the broad-band nature of the propagated signals, the information carried by low wavenumbers extends to negative offsets even though our cylindrical coordinate system considers only positive offsets. Large, positive wavenumbers affect only positive offsets for which the $\mathcal{F}_2(k, L)$ filter introduced in eq. (23) is unambiguously defined. This is no longer the case with small, positive wavenumbers which mix data requiring both the $\mathcal{F}_2(k, L)$ and the $\mathcal{F}_2(-k, L) = -\mathcal{F}_2(k, L)$ filters, which differ by their sign. This distinction cannot be made in the $f - k$ domain. One way of solving this problem would be to replace the integration scheme with respect to radial wavenumber

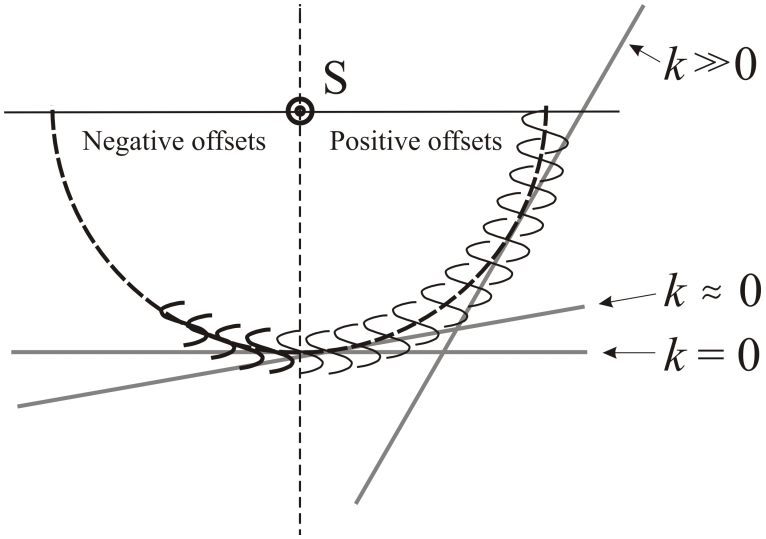

Figure B.1 Construction of a circular wavefront radiated by a source S with broad-band frequency content through superimposition of plane waves described by their wavenumber k. Low wavenumber contributions integrate information belonging to the negative offset domain.

k in eq. (22) by the two-dimensional positive and negative (k_x, k_y) wavenumber integration introduced by Bouchon (1979), which is more flexible in its application but requires more computation time.

The wavenumber response of 3-electrode arrays is the even function $\mathcal{F}_3(-k, L) = \mathcal{F}_3(k, L)$. This filter correctly handles the situation described above at all wavenumbers.